Journal of Alloys and Compounds 947 (2023) 169585

Contents lists available at ScienceDirect

Journal of Alloys and Compounds

journal homepage: www.elsevier.com/locate/jalcom

Influence of the calcination duration of g-C_3N_4/TiO_2 "veggie-toast-like" photocatalyst on the visible-light triggered photocatalytic oxidation of bisphenol A

Matevž Roškarič [a], Gregor Žerjav [a,*], Matjaž Finšgar [b], Janez Zavašnik [c], Albin Pintar [a]

[a] Department of Inorganic Chemistry and Technology, National Institute of Chemistry, Hajdrihova 19, SI-1001 Ljubljana, Slovenia
[b] University of Maribor, Faculty of Chemistry and Chemical Engineering, Smetanova ulica 17, SI-2000 Maribor, Slovenia
[c] Gaseous Electronics, Jožef Stefan Institute, Jamova cesta 39, SI-1000 Ljubljana, Slovenia

ARTICLE INFO

Article history:
Received 6 December 2022
Received in revised form 2 March 2023
Accepted 7 March 2023
Available online 10 March 2023

Keywords:
G-C_3N_4/TiO_2 photocatalyst
Calcination time
Photocatalysis under visible-light illumination
Water remediation
Bisphenol A

ABSTRACT

Two commercially available TiO_2 (hexagonal-like and spherical-like particles) were used to investigate the effect of g-C_3N_4 "melting" on the photocatalytic properties of g-C_3N_4/TiO_2 composites. Improvement in the contact between the components was observed when they were thermally treated at 350 °C for an extended period of time (between 2 and 72 h) due to the partial melting and phase fusion of g-C_3N_4. Consequently, the enhanced contact between the phases allows easier injection of photogenerated electrons from the conduction band of g-C_3N_4 into TiO_2, improving charge carrier separation. The prepared composites were tested for bisphenol A degradation under visible-light illumination, which showed that the components that had been calcined for 24 h performed better due to the improved charge carrier separation. Superoxide anionic radicals and photogenerated holes were identified as active species in the photooxidation experiments conducted under visible-light illumination.

1. Introduction

Due to its low cost, unique optical properties and high photochemical stability, titanium dioxide (TiO_2) is one of the most commonly used semiconductors as photocatalysts. However, it has two major drawbacks that limit its usage in applications where visible- or solar-light illumination is used: (i) a high rate of electron-hole pair recombination, and (ii) a wide band gap value (3.0–3.4 eV) [1–4]. To improve or overcome the limiting properties of TiO_2, different methods and modifications can be used: a combination of different TiO_2 polymorphs, using different morphologies of TiO_2, doping TiO_2 with metals or non-metals, impregnating TiO_2 with plasmonic metals (Au, Ag, Pt, etc.) or combining TiO_2 with other suitable low band gap semiconductors [1,2,4–11]. Previously, attention has been drawn to the use of the green semiconductor graphitic carbon nitride (g-C_3N_4), which contains only earth-rich elements, such as carbon and nitrogen, in AOPs [2,12]. The benefits of g-C_3N_4 are its relatively high chemical stability and moderate band gap value, making it suitable for visible-light absorption [2,13–16]. The applicability of g-C_3N_4 as a photocatalyst in AOPs is limited by its two major drawbacks: (i) low specific surface area, and (ii) fast charge carrier recombination [2,6,14,17]. To overcome the drawbacks of TiO_2 and g-C_3N_4, it is advantageous to synthesize g-C_3N_4/TiO_2 composites to form a junction between them [16,18,19].

Several synthesis parameters have an effect on the activity of composite photocatalysts, such as the calcination temperature and time [20–22]. Only a few authors have studied the effect of calcination time or the combined effect of calcination time and temperature on their composite photocatalysts. Reli et al. [23] studied the effect of calcination temperature (600–750 °C) and time (1–3 h) on the kaolinite/TiO_2 composite for the photocatalytic reduction of CO_2 under UV-light illumination. They found that the prolongation of the calcination time at an elevated temperature (600 °C) increased the crystallite size of the kaolinite/TiO_2 composite, leading to the increased crystallinity of the powder. The increase of the crystallite size improved the activity of kaolinite/TiO_2 photocatalysts, as the phase composition and specific surface area remained nearly the same. Mouele et al. [24] studied the effect of different pyrolysis times (105–135 min) at 350 °C on the properties of carbon and nitrogen co-doped TiO_2. They found that the pyrolysis time affects the carbon content, which in turn influences the TiO_2 band gap, particle size and morphology, as well as the electronic properties. With the increase of the pyrolysis time, the carbon and nitrogen content decreased due to thermal evaporation. Consequently, the beneficial

* Corresponding author.
E-mail address: gregor.zerjav@ki.si (G. Žerjav).

https://doi.org/10.1016/j.jallcom.2023.169585

effect of the carbon and nitrogen doping was decreased, reducing the photocatalytic activity. Zhang et al. [25] studied the effect of the calcination time (1–5 h) on the structure and activity of the photocatalyst TiO_2-Al_2O_3. They found that a calcination time of 3 h greatly improved the photocatalytic activity of methyl orange degradation (77.0%) under UV-light illumination. Additionally, 3 h calcination improved the composite photocatalytic adsorption properties, as the total dye decolouration was 95.1% in the 90 min reaction timespan.

The main objective of the present study was to propose a novel "toast"-like concept of the g-C_3N_4/TiO_2 composites, where g-C_3N_4 has the role of "cheese", TiO_2 the role of "bread" and the calcination oven the role of a "toaster". To gain new insights into the effects of g-C_3N_4 (cheese) "melting" on the morphological, electronic and photocatalytic properties of "toast"-like g-C_3N_4/TiO_2 composites, the calcination time in the final calcination step (toaster) of the synthesis procedure was prolonged up to 72 h. To the best of the authors' knowledge, no studies have been performed investigating the effect of calcination time in g-C_3N_4/TiO_2 systems. In this work, the g-C_3N_4/TiO_2 composites were prepared using a simple mortar synthesis in which we combined the prepared g-C_3N_4 (CN) with one of the two morphologically different commercial TiO_2 nanoparticles (spherical (TP) or hexagonal (TH)) and varied the duration of the final calcination step (350 °C in air) from 2 to 72 h. By using various characterization methods, we gained several new insights into the junction formed between the two components and how it is affected by the calcination duration and the type of TiO_2. In addition, the photocatalytic activity of the produced materials was studied in a slurry batch reactor using an aqueous solution of the endocrine-disrupting compound bisphenol A (BPA) as a model organic pollutant. Furthermore, the results of the study indicate the characterization techniques that are suitable and necessary to fully evaluate the photocatalytic properties of a series of photocatalysts g-C_3N_4/TiO_2.

2. Experimental

2.1. Synthesis of materials

All the chemicals used for the synthesis were of analytical grade and used without further purification. In all cases, 18.2 MΩ cm ultrapure water (Elga Purelab Flex) was used. Dicyandiamide (Sigma Aldrich) was used to synthesize g-C_3N_4 by applying the following calcination procedure: heating from room temperature with a ramp of 300 °C/h to an end temperature of 550 °C, which was held for 4 h. After cooling, the obtained yellow solid was ground in a mortar and denoted as CN. Two different commercially available TiO_2 powders were used for the composite photocatalysts: DT-51 (CristalACTiV™), denoted as TP, and TiO_2-1 (XT25376, Saint-Gobain), denoted as TH. A facile procedure was used for the g-C_3N_4/TiO_2 composite synthesis. First, both components were mixed in a mortar with a weight ratio of 1:1 to obtain CNTP-M and CNTH-M samples. Afterwards, the CNTP-M and CNTH-M solids were calcined in a muffle furnace at 350 °C in the air with a ramp of 300 °C/h for either 2, 8, 24 or 72 h. The TP series materials were denoted CNTP-2, CNTP-8, CNTP-24 and CNTP-72, and the TH series CNTH-2, CNTH-8 and CNTH-24. Pure CN samples were also calcined at the same conditions as the composites and denoted CN-2, CN-8 and CN-24.

2.2. Structural and textural properties of the materials

A Perkin Elmer FTIR Frontier spectrometer equipped with a Perkin Elmer sample holder for pellets was used for the transmission FTIR measurements. The sample compartment was purged with nitrogen. The pellets were prepared as follows: 1 mg of the sample was thoroughly mixed in a mortar with 600 mg of KBr. After mixing, 1/3 of the mixture was put in a sample holder (13 mm diameter) and pressed with 49 kN for 40 s to prepare the pellet. For all spectra, an average of 40 scans was used in a range between 4000 and 450 cm^{-1} and a spectral resolution of 4 cm^{-1}.

The phase composition and purity of the investigated samples were determined using the PANanalytical PRO MPD diffractometer. The specific surface area, pore volume and average pore size were determined by nitrogen physisorption analysis using Micromeritics TriStar II 3020. Details about the measurement procedures can be found in [10].

Acidic surface sites were determined using pyridine (Merck) as a probe molecule and a Perkin Elmer Pyris 1 TGA analyser equipped with a platinum sample cell. The measurements were carried out using the following protocol: heating from 50° to 125°C at 10 °C/min and holding at 125 °C for 15 min in a stream of air. Afterwards, the samples were cooled to 120 °C at 10 °C/min with a switch to a nitrogen stream of 50 mL/min. The total duration of that step was 130 min. During that time, pyridine valves were opened to saturate the sample for 10 min. The desorption of pyridine was carried out from 120° to 360°C at 20 °C/min in a stream of nitrogen. We also performed the long-term TGA measurement of the CNTP-M catalyst, which was kept at 350 °C for 72 h in the air (50 mL/min).

The CO_2 temperature-programmed desorption (CO_2-TPD) profiles of the investigated samples were obtained by heating the sample in an O_2 (5%)/He stream (20 mL/min) from room temperature to 125 °C (10 °C/min) in the Micromeritics AutoChem II 2920 apparatus. After 10 min, the samples were cooled to 50 °C, followed by switching the gas stream to Ar (20 mL/min). CO_2 was introduced onto the sample by dosing pulses of CO_2 (80 vol%)/Ar into the Ar stream (20 mL/min), which flowed through the samples at 50 °C. Desorption of CO_2 from the sample into the Ar stream (20 mL/min) was monitored in the temperature range of 50–360 °C (heating ramp 10 °C/min).

Zeta potential measurements were performed using a Malvern Panalytical zetasizer Ultra Red, equipped with a Malvern multipurpose titrator MPT-3. Hydrochloric acid (HCl, 0.25 and 0.025 M) and sodium hydroxide (NaOH, 0.25 M) solutions were used to adjust the pH value in the measured range. All samples were purged with 50 mL/min of nitrogen (Linde, purity 5.0). To prepare the initial suspension for the pH-dependent zeta potential measurements, 25 mg of the photocatalyst was dispersed in 100 mL of ultrapure water with medium stirring for 30 min. To determine the average particle size utilizing dynamic light scattering using the same instrument, 25 mg of a sample was dispersed in 250 mL of ultrapure water and stirred for 30 min. The measurements were carried out for three different sample solutions to obtain an average value.

The morphology and chemistry/phase composition of the prepared nanosolids were investigated employing a field-emission scanning electron microscope (FE-SEM) Carl Zeiss model SUPRA 35 VP and transmission electron microscope (TEM, JEM-2100, JEOL Inc.). The details about the operating conditions are provided in [10].

2.3. Determination of the elemental composition of the materials

The weight content of carbon, hydrogen and nitrogen in the fresh and used photocatalysts was determined using a Perkin Elmer CHNS analyser (model 2400 Series II).

XPS analyses were performed with the Supra+ instrument (Kratos Analytical, Manchester, UK) using a hemispherical electron analyser, Al K_α excitation source and a monochromator. During the XPS data acquisition, the charge neutralizer was turned on. The analysis spot size was 300 by 700 micrometers, and the analysis was performed at a take-off angle of 90°. High-resolution spectra were measured at 20 eV pass energy. Data acquisition and processing were performed with ESCApe 1.4 (Kratos, Manchester, UK). The binding energy scale was corrected using the C-C/C-H peak at 284.8 eV in the C 1 s spectrum (or at 288.2 for g-C_3N_4 if C-C/C-H was missing).

2.4. Analysis of the optical and electronic properties of materials

A Perkin Elmer Lambda 35 UV-Vis spectrophotometer and Perkin Elmer LS-55 fluorescence spectrometer were used to measure UV-Vis diffuse reflectance (DR) and solid photoluminescence (PL) spectra. Detailed information about the measurement settings can be found in [10]. Electrochemical impedance spectroscopy (EIS) analysis was performed using a potentiostat/galvanostat (Methrom Autolab, model PGSTAT302N) equipped with an EIS module FRA32M. Details about the preparation of the working electrode and measurement settings are provided in [5,7].

2.5. Tests of reactive oxygen species generation by the prepared materials

To determine the hydroxyl radical (·OH) formation tendency of the prepared materials, a photoluminescence method was used in combination with the probe molecule coumarin (Alfa Aesar). Details about the experimental setup and determination of the 7-hydroxycoumarin concentration can be found in [10]. To monitor the generation of photogenerated electrons (e^-) and/or superoxide anionic radicals (O_2^-), 17.2 mg of 2,2´-azino-bis(3-ethylbenzothiazoline-6-sulfonic acid) (ABTS, Sigma) and 3.3 mg of $K_2S_2O_8$ (Aldrich) were dissolved in 5 mL of ultrapure water and mixed for 16 h in the dark at room temperature. To prepare the reaction mixture, 1 mL of the above-mentioned ABTS+$K_2S_2O_8$ solution was dissolved in 50 mL of ultrapure water to prepare the reaction $ABTS^{·+}$ solution. 10 mg of the photocatalyst was suspended in the prepared solution at 400 rpm. To obtain the adsorption/desorption equilibrium, a 30 min dark period was applied. A Schott KL 1600 LED light source equipped with a UV cut-off filter at 410 nm was used to trigger the photocatalytic activity of the examined materials to generate e^- and/or O_2^-, which decolourized the green $ABTS^{·+}$ radical solution. Liquid-phase samples were withdrawn at specific time intervals in the 180 min timespan of the reaction and filtered through a 0.2 µm regenerated cellulose membrane (Chromafil® RC-20/25). One drop of the liquid-phase sample was put on a Hellma TrayCell that was inserted into the sample compartment of the Perkin Elmer Lambda 45 UV-Vis spectrophotometer. A Hellma TrayCell cap with an optical dilution factor of 5 was used to perform the measurements. In the recorded UV-Vis spectra, the peak at 345 nm belongs to ABTS, and the peaks at 395 and 410 nm belong to the $ABTS^{·+}$ radical cation radical, which were used to obtain the reaction curves.

2.6. Tests of the photocatalytic activity of the prepared materials

The details about the photocatalytic experiments where the endocrine-disrupting compound bisphenol A (BPA, Aldrich) was used as a model organic pollutant are provided in [10]. For the reactive oxygen species "quenching" experiments, we used p-benzoquinone (BQ, Sigma Aldrich), sodium azide (NaN_3, Merck), methanol (MeOH, Baker) and formic acid (HCOOH, Kemika) as traps for O_2^-, $^1O_2$,·OH, and h^+, respectively. In all cases, the trap concentration was 10 mM using the same experimental set-up as for the photooxidation of only BPA.

The temporal BPA concentration in the withdrawn aqueous-phase samples was measured using a Shimadzu HPLC LC-40 instrument equipped with a 100 × 4.6 mm BDS Hypersil C18 (2.4 µm) column. The mobile phase was a mixture of methanol (Baker) and ultrapure water (70:30 vol ratio) with a flow rate of 0.5 mL/min. The column was thermostated at 30 °C and the autosampler at 25 °C. The detection of BPA was carried out with a PDA detector from 190 to 350 nm with a flow-through cell temperature of 40 °C.

The total organic carbon (TOC) content was determined in fresh and treated BPA solutions using a Shimadzu TOC-L instrument equipped with an ASI-L autosampler. Synthetic air (Messer, purity 5.0) was used as a carrier gas in the analyser operating at 680 °C to perform the high-temperature catalytic oxidation of organics present in the injected samples. The CO_2 formed was quantified by a calibrated NDIR detector. The observed error of three repetitions was within ± 1%. Furthermore, utilizing the PerkinElmer CHNS 2400

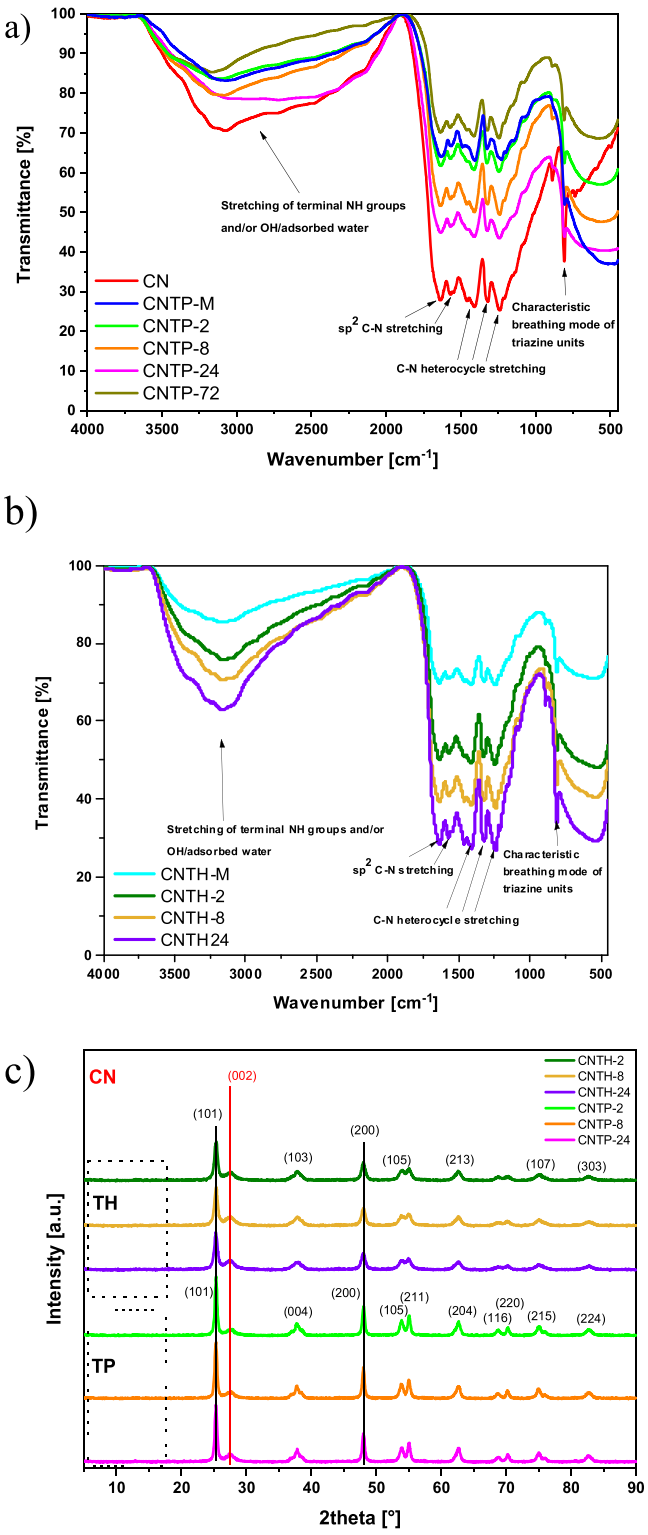

Fig. 1. FTIR spectra for sample/KBr pellets for (a) the CNTP series and (b) the CNTH series of samples and XRD patterns for the CNTP and CNTH series of investigated materials (c). The black solid lines represent the characteristic peaks for anatase TiO_2 (TP PDF JCDD 00–021–1272 and TH PDF JCDD 01–086–1157)) and the red solid line the characteristic peak of g-C_3N_4 (PDF JCDD 00–066–0813).

Series II analyser, we determined the extent of the carbon deposition on catalyst samples after the photocatalytic oxidation reactions and calculated the real mineralization.

3. Results and discussion

3.1. Structural and textural analyses

To confirm the successful synthesis of g-C_3N_4 (CN) and its incorporation into the composite photocatalysts, transmission FTIR measurements were performed. In Figs. 1a and 1b, the peaks at 1234, 1327 and 1410 cm^{-1} can be assigned to C-NH-C stretching, and the peaks at around 1567 and 1636 cm^{-1} can be assigned to the C═N heterocycle vibration modes in the g-C_3N_4 materials. The peak at 808 cm^{-1} corresponds to the characteristic breathing mode of the triazine unit of g-C_3N_4 materials [26,27]. A broad peak centred at 3167 cm^{-1} corresponds to either surface-adsorbed water/hydroxyl functional groups or functional groups still left from the polycondensation [26,27]. Regardless of the TiO_2 used, in all cases of the prepared composites, we can observe the entire characteristic peaks belonging to g-C_3N_4. Furthermore, the positions and shape of peaks did not change, which means that the synthesis procedure did not affect the structural properties of the g-C_3N_4 material. A baseline slope is observed at higher wavenumbers due to the scattering of the infrared light at the sample surface or interior [28]. In addition, in all the composite photocatalysts (CNTP and CNTH), we observe a new peak between 800 and 450 cm^{-1}, corresponding to Ti-O-Ti stretching [29]. The presence of the characteristic peaks of both components is a good indication of a successful synthesis of heterostructured photocatalysts.

With the prolongation of the calcination time up to 24 h (Fig. 1a and b), the transmittance intensity decreased and again increased with the 72 h calcination. The decrease of the transmittance intensity could indicate that a better contact between the components was established as the samples could become “denser”, which in turn increased the chances for the materials (characteristic bonds) to absorb IR light. Additionally, with the prolongation of calcination time, the decomposition of CN increases; thus, the transmittance intensity of the material increases (CNTP-72) as less characteristic bonds are present. To further study this effect, we also performed a FTIR analysis of pure CN materials, calcined for different calcination times. From the results in Fig. S1a, we can observe that the transmittance intensity for pure CN photocatalysts did not change significantly with the prolongation of the calcination time. Therefore, we can almost certainly ascribe the changes in the transmittance intensity to forming a better junction between the components, since the interaction between both components is needed as a driving force to generate this effect.

To identify the carbonaceous phase and the polymorph of TiO_2, we performed XRD measurements of the investigated photocatalysts (Fig. 1c and S1b). We can observe that both TiO_2 samples exhibit characteristic peaks for anatase TiO_2 (PDF JCDD 00–021–1272 for the TP samples and PDF JCDD 01–086–1157 for the TH solids). In all the investigated composites, only (002) peak at 27.5° 2θ appeared that corresponds to the characteristic peak of g-C_3N_4 for the inter-planar stacking of graphite-like materials (PDF JCDD 00–066–0813) [34–36]. The characteristic (100) peak for the plane of the tri-s-triazine unit of g-C_3N_4 at around 13.2° 2θ was not observed due to the low crystallinity of the CN component [16,30–32]. However, for all pure CN photocatalysts calcined for different durations at 350 °C, both the characteristic peaks for g-C_3N_4 are visible (Fig. S1b). The composite synthesis approach did not significantly affect the TiO_2 components, as their peak positions and shape did not change (Fig. 1c). However, some minor changes in the composite photocatalyst for the peak belonging to g-C_3N_4 are observed. The first observation is that the content of g-C_3N_4 is decreasing, which correlates with the lowering of the peak intensity at 27.5° 2θ [18,33]. Additionally, the lower peak intensity could be due to strong interactions between the components, thus destroying the interlayer stacking of CN and reducing its crystallinity, which is in agreement with the results of the research performed by Feng et al. [34] where g-C_3N_4/CdS photocatalyst was investigated. We can speculate that this phenomenon is observed due to the favourable electronic properties of the two components, which can interact when the heterojunction is formed. In our investigated “toast”-like g-C_3N_4/TiO_2 composites, a heterojunction formation was suggested by the results of FTIR and XRD measurements. A second observation is that if we compare the peak positions of g-C_3N_4 at 27° 2θ for the pure CN (27.67°) and composites (2–24 h), we can observe a slight shift from 27.53° to 27.30° 2θ for the CNTP series and from 27.56° to 27.50° 2θ for the CNTH series. This shift was also observed in the study of g-C_3N_4-TiO_2 photocatalysts performed by Li et al. [35], where they stated that this could indicate a closer interaction between the phases. It may originate from a partial “phase fusion” of the two components, thus slightly changing the crystalline properties of the samples, which is also consistent with the reduction of the g-C_3N_4 peak at 27° 2θ. Using the Scherrer equation for spherical particles, we estimated the crystallite size (Table 1) of TiO_2 from (101) and (200) peaks as 17.4 and 18.6 nm for the TP sample and 23.4 and 11.1 nm for the TH solid, while for pure CN, the crystallite size equals 3.8 nm (based on (002) peak). The TiO_2 crystallite size remains the same or increases only to a limited degree during the composite synthesis. On the other hand, the crystallite size for the g-C_3N_4 component increases, as would be expected with the improvement of the contact area, whereas g-C_3N_4 with its relative thermal (in) stability would act as a binder between the components (“like cheese in a toasted sandwich”). However, as the CN component is a 2D material and therefore its estimation with the Scherrer equation for spherical particles leaves space for error, the increase of g-C_3N_4 crystallite size could originate due to the uncertainty of the used estimation method.

Nitrogen physisorption analysis was performed to gain information about the porosity of the prepared composites. From Fig. S2, we can conclude that all the synthesized photocatalysts exhibit type IV(a) isotherms with H3 hysteresis loops, which indicates a mesoporous structure with slit-like pores [33,36,37]. However, for the CNTH series, we observed some overlapping of the H2 and H3 loops, indicating a mesoporous structure within the TH carrier [33]. From the results in Table 2, we can observe that pure g-C_3N_4 has a characteristic low specific surface area of 12.3 m^2/g [6]. As seen for the CNTP-M (52.0 m^2/g) and CNTH-M (80.1 m^2/g) photocatalysts, the addition of TiO_2 increases the specific surface area. However, the calcined composites exhibit a decrease in the specific surface area

Table 1
Estimated crystallite sizes for TiO_2 components at 25 and 48° and for g-C_3N_4 components at 27° using the results of the XRD analysis and the Scherrer equation for spherical particles and the g-C_3N_4 peak position for the peak at around 27°.

Sample	Crystallite size @ 25°	Crystallite size @ 48°	Crystallite size @ 27°	g-C_3N_4 peak position
	nm			°
CN	-	-	3.8	27.666
TP	17.4	18.6	-	-
CNTP-M	17.4	18.6	6.5	27.461
CNTP-2	17.4	18.6	7.4	27.529
CNTP-8	17.4	22.4	8.7	27.430
CNTP-24	17.4	22.4	9.6	27.298
CNTP-72	17.4	22.4	10.4	26.935
TH	23.4	11.1	-	-
CNTH-M	21.1	12.3	6.5	27.557
CNTH-2	23.3	13.9	7.4	27.562
CNTH-8	23.2	13.9	8.7	27.509
CNTH-24	23.4	13.9	10.4	27.496

Table 2
Results of N_2 adsorption/desorption experiments (specific surface area (S_{BET}), pore volume (V_{pore}) and average pore diameter (d_{pore})), estimated band gap values from UV-Vis-DR measurements using the Kubelka-Munk theory and the charge transfer resistance (R_{CT}) obtained from the Nyquist plot fitted into the equivalent electrical circuit.

Sample	S_{BET}	[a]V_{pore}	d_{pore}	Band gap	R_{CT}
	m^2/g	cm^3/g	nm	eV	MΩ
CN	12.3	0.05	16.2	2.61	0.83
TP	89.4	0.31	14.1	3.28	0.96
CNTP-M	52.0	0.21	16.3	3.09	0.74
CNTP-2	63.3	0.24	14.9	3.14	0.48
CNTP-8	56.9	0.22	14.9	3.16	0.44
CNTP-24	53.9	0.20	14.9	3.16	0.40
CNTP-72	59.1	0.23	15.4	3.20	-
TH	146.0	0.39	10.8	3.26	0.86
CNTH-M	80.1	0.21	10.9	2.99	0.74
CNTH-2	83.6	0.26	12.3	3.04	0.65
CNTH-8	79.5	0.24	11.9	3.08	0.63
CNTH-24	78.8	0.24	12.2	3.09	0.60
CN-2	12.0	0.04	16.1	2.61	-
CN-8	11.8	0.04	15.9	2.64	-
CN-24	11.5	0.03	15.3	2.61	-

[a] The listed values determined by means of N_2 physisorption measurements consider micro- and mesopores, as well as macropores up to 300 nm.

when prolonging the calcination time from 2 to 24 h, from 63.2 to 53.9 m^2/g for the CNTP series and from 83.6 to 78.8 m^2/g for the CNTH series of composites. The reason behind this behaviour is the improvement of the contact between the components, as g-C_3N_4 is relatively thermally (un)stable even at 350 °C. Prolonging the calcination time at 350 °C increases the decomposition and "melting" of the g-C_3N_4 component, forming a better junction with TiO_2. This decreases the specific surface area of the composites, although, as seen in the CNTP-72 sample, the specific surface area can increase again due to the loss of the CN component. There is no effect of the calcination time of the pure CN series on the values of the specific surface area.

To obtain information on the surface acidic and basic sites [38], we performed Pyr-TPD and CO_2-TPD experiments. From Table S1, we can conclude that the majority of the acidic surface sites come from TiO_2; however, basic surface sites are equally present in g-C_3N_4 and TiO_2. In the composite photocatalysts, the prolongation of the calcination time increases the acidic surface sites for the CNTP series and slightly decreases for the CNTH series. In contrast, the CNTP series exhibits a slight decrease in basic surface sites with the prolongation of calcination time. This phenomenon is due to the decomposition and "melting" of g-C_3N_4 components and is described more thoroughly in the Supplementary Information. As the overall changes to these properties are slight with the prolongation of the calcination time, its effect on the photocatalytic activity will probably be minor. Employing the zeta potential measurements, we obtained the point of zero charge (pH_{PZC}) for the investigated photocatalysts. From the results in Table S1, we can observe that the synthesized photocatalysts exhibited pH_{PZC} values in the range of 4.12–5.55, which is typical for nonpolar graphite-like materials ($pH_{PZC} \sim 4$), as it is g-C_3N_4 in our case [39,40]. A decrease in pH_{PZC} values was observed with the prolongation of calcination time, which could indicate an improved contact between the phases [40]. The improved contact was also suggested from the particle size measurements, where the distribution of the particle size changed from the dual distribution (as for pure TP) to a more uniform, probably due to the binding effect of the CN component (for further information, see Supplementary Information file).

The in-depth interaction of both phases was assessed using SEM analysis (Fig. S4) and TEM analysis (Fig. 2). In all samples, g-C_3N_4 and TiO_2 components are observed in all composites (Fig. 2), forming larger aggregates. Further, we can observe that the CN component has a large, irregular canvas-like shape, which binds together the TP/TH particles. The role of CN here can be analogous to the role of "cheese" in a toasted "veggie" sandwich, which binds together the ingredients. A slightly more defined CN structure is present when the calcination synthesis is applied. The origin of this lies in the relative thermal (in)stability of the g-C_3N_4 material: already heating at 350 °C for a prolonged time can affect the g-C_3N_4 morphology. Nevertheless, no other major changes were observed in the morphologies of the CN components, as 350 °C is not high enough to thermally exfoliate CN to a fully sheet-like structure, which typically requires a calcination temperature of at least 450 °C [41–43]. No changes were observed for the TP particles, which appear in a spherical-looking shape. The average particle size of the TP was constant during the synthesis (13.9 nm, Table S2), and their particle size distribution remained the same (Fig. 3), which is consistent with the XRD analysis. From the comparison of the experimental selected area electron diffraction (SAED) patterns (Fig. 2) and the simulated patterns, we can conclude that TiO_2 is only present in the anatase form in all the investigated CNTP materials. In the case of the CNTH series, similar results are obtained as for the CNTP series, except that the CN structure seems more defined, even in the mortar synthesis approach, which could have a beneficial effect on the photocatalytic activity. Nevertheless, the CN component again acts like a binder ("cheese") in the composite photocatalyst. This is seen in comparing the distance between the TH particles in CNTH-M, which seems to be larger than in the case of the CNTH-24. A prolonged calcination time could result in better contact between the components, as suggested by the results of other textural and surface analyses. From Fig. 2, we can observe that the TH particles are not solely hexagonal as stated by the manufacturer, and other morphologies are present. However, the particle size and distribution did not change significantly (9.8–10.7 nm), regardless of the synthesis approach used – except for the case of the CNTH-24 sample, in which we observed a minor increase (10.7 nm) in comparison to the CNTH-M solid (9.8 nm). The comparison of the recorded SAED patterns of the CNTH series with the simulated SAED patterns (Fig. 2) confirms that also in the CNTH series, only the anatase TiO_2 polymorph is present. At the same time, the carboniferous phase is manifested as a broad, continuous ring typical for near-amorphous materials. Indeed, the TEM micrographs of the carbon phase recorded at high magnification show an amorphous structure without long-range ordering. The increased thickness of the particle edges and around embedded TiO_2 nanoparticles suggest partial melting of the carboniferous (g-C_3N_4) phase, increasing the contact between phases as seen in the high magnification TEM figure (marked by yellow arrows in Fig. 2). The heating process that fused CN and TP particulates mixture was performed by annealing at 350 °C; below the pyrolysis temperature of CN. The full thermal process of powder compacts to solid hard components by melting of the matrix-forming binding elements takes place in 3 main stages: (i) bound growth starting, (ii) shrinkage of pores, and (iii) formation of grain boundaries. In our case, only the 1st stage was achieved, and diffusion of the CN phase by necking around TP particles occurred (Figs. S5 a-c), which resulted in partial phase fusion and increased contact between both phases, affecting the heterojunction.

To confirm the possible "melting" of the CN component and its role as "cheese" in the "toast"-like g-C_3N_4/TiO_2 composite, we performed the TGA measurement in the air for the CNTP-M sample for 72 h at 350 °C to simulate the synthesis conditions. As shown in Fig. S5d, the weight loss after 72 h at 350 °C is minimal (< 3%), most likely due to water evaporation and some minor CN decomposition. However, the vast majority of the CN component is still present after

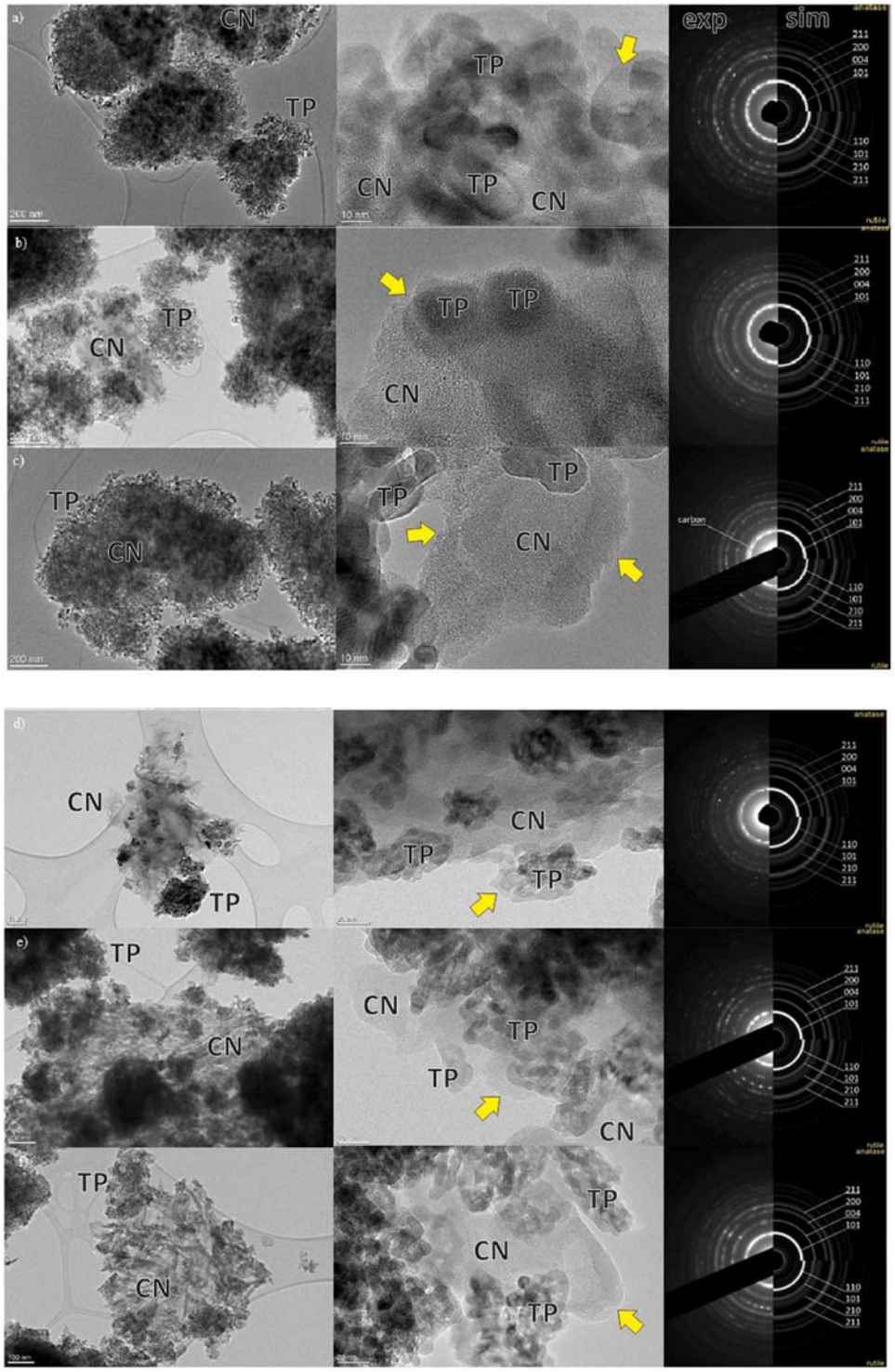

Fig. 2. An overview and high-magnification TEM micrographs with corresponding experimental selected area electron diffraction (SAED) patterns, compared with the ab-initio simulations for anatase and rutile TiO_2 polymorph. Results for CNTP-M (a), CNTP-2 (b), CNTP-24 (c), CNTH-M (d), CNTH-2 (e) and CNTH-24 (f) samples. CN stands for the g-C_3N_4 and TP for the TiO_2 phase. Arrows mark the thickened CN edges due to partial melting.

72 h in contrast to the real system, where some weight loss of CN compound was observed (explained in the following chapters). Considering the results of TEM and TGA analyses, we can tentatively assume that the CN component indeed "melted" to some degree, thus decreasing the distance between TP and TH particles and improving the contact between the phases. This will affect the optical and electronic properties of the composites and will be discussed in detail in the following sections.

3.2. Elemental analysis

The CHNS elemental analysis of fresh materials (Table S3) shows that all the composites contain carbon, hydrogen and nitrogen, which originate from g-C_3N_4 and/or from surface-adsorbed components of air (CO_2 and N_2). Therefore, an absolute determination of the content of the CN component in the composites using this technique is not possible, though the results can be used for an

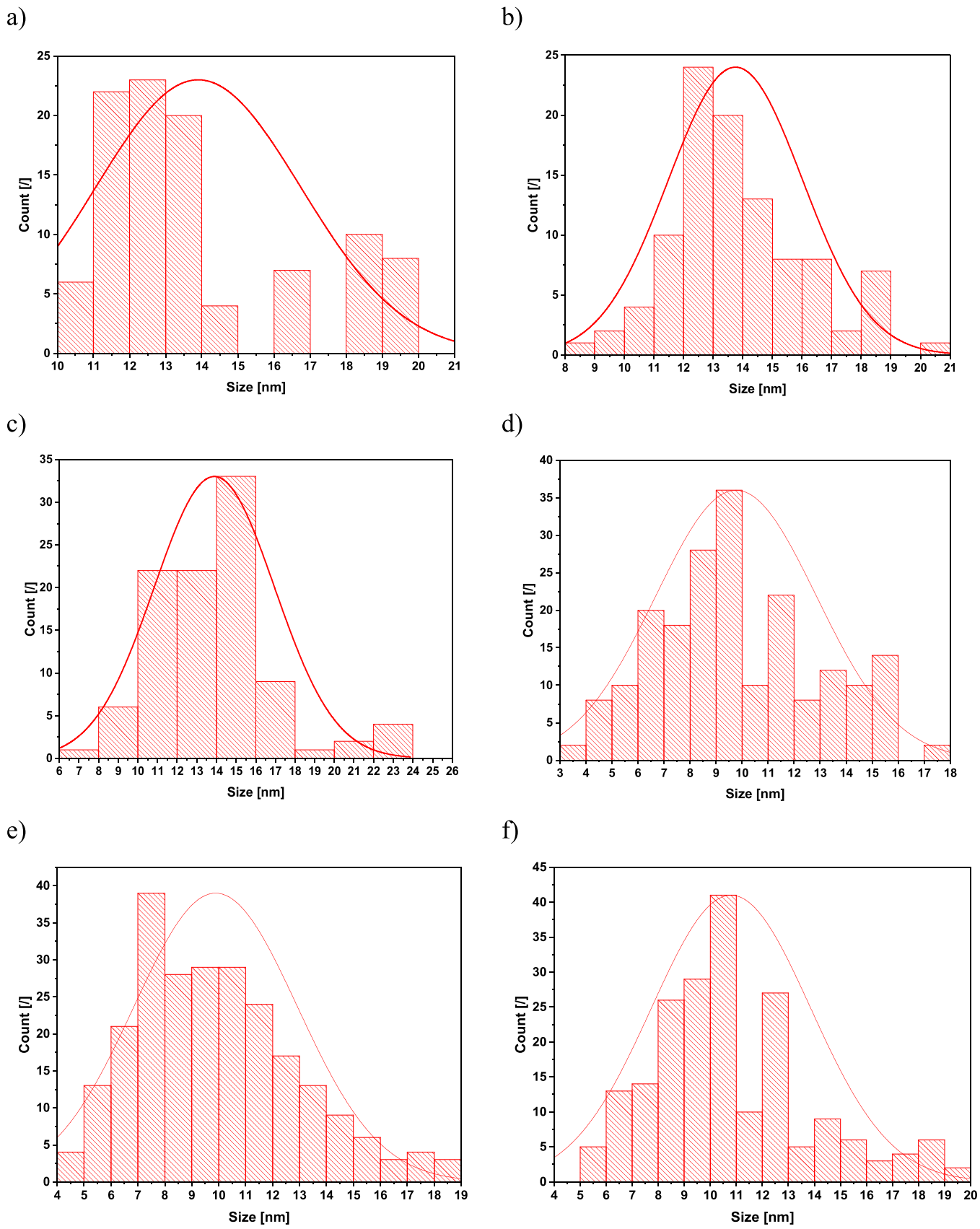

Fig. 3. Size distribution of 100 measured TiO_2 nanoparticles obtained from TEM micrographs for CNTP-M (a), CNTP-2 (b), CNTP-24 (c), CNTH-M (d), CNTH-2 (e) and CNTH-24 (f) samples.

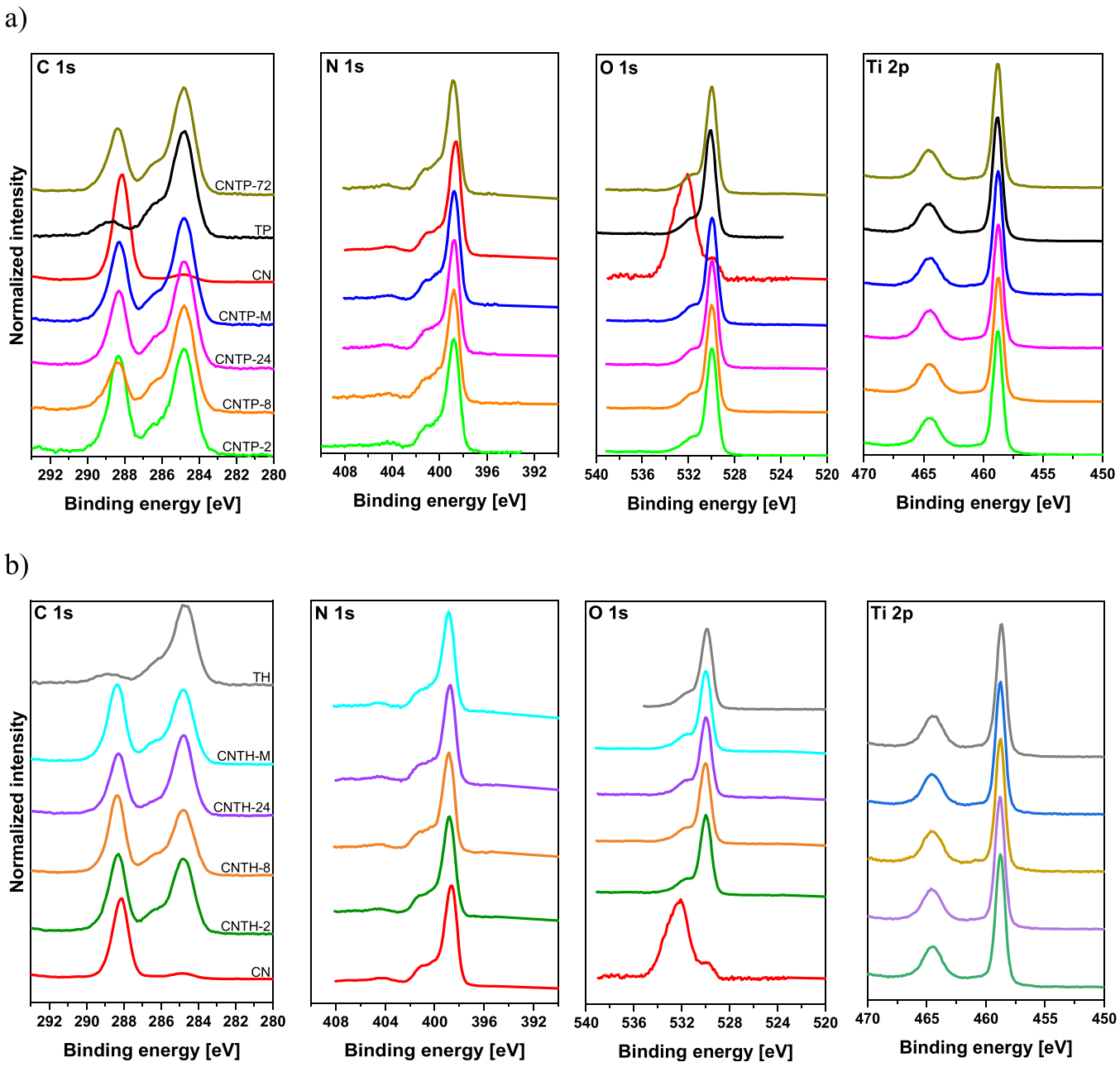

Fig. 4. High-resolution C 1 s, N 1 s, O 1 s and Ti 2p XPS spectra for the CNTP (a) and CNTH (b) series of samples.

estimation. The CNTP-M and CNTH-M samples exhibited a similar content of the CN component (46.4 and 44.7 wt% of carbon and nitrogen). Prolonged duration of the calcination of the mortared composites at 350 °C results in a decrease in the carbon and nitrogen content. The origin of this phenomenon lies in the thermal decomposition of g-C_3N_4, which is most exhibited in the case of the CNTP-72 sample with the longest investigated calcination time. The elemental analysis confirms the suggested decrease of the weight content for the CN component in the composites with the prolongation of calcination time.

The XPS survey spectra and high-resolution XPS spectra are illustrated in Figs. S6 and 4 for the CN component and the corresponding mortar and calcined composites using TP and TH, respectively. The C 1 s spectrum (Fig. 4) for CN shows a main peak at 288.2 eV corresponding to the C-N in g-C_3N_4. This spectrum also contains low-intensity features for C-C/C-H and C-O containing species originating from adventitious carbonaceous species (Fig. S6c). The C 1 s spectra for the TP and TH samples show an intense peak for C-C/C-H and a low-intensity shoulder corresponding to C-O (both originating from adventitious carbonaceous species). All other C 1 s spectra for mortar and calcined composites show two main spectral features corresponding to C-C/C-H (from adventitious carbonaceous species) and g-C_3N_4. A high binding energy shoulder of the C-C/C-H peak corresponds to C-O originating from oxidized adventitious carbonaceous species. Generally, the C-1 s spectra in Figs. 4 and S6c for mortar and calcined composites have similar shapes and positions of the main peaks, indicating a similar C environment. The high-resolution N 1 s spectra (Fig. 4) consist of the intense feature at 398.5 eV corresponding to the g-C_3N_4 material. The high binding energy shoulder corresponds to -NH_2 or =NH

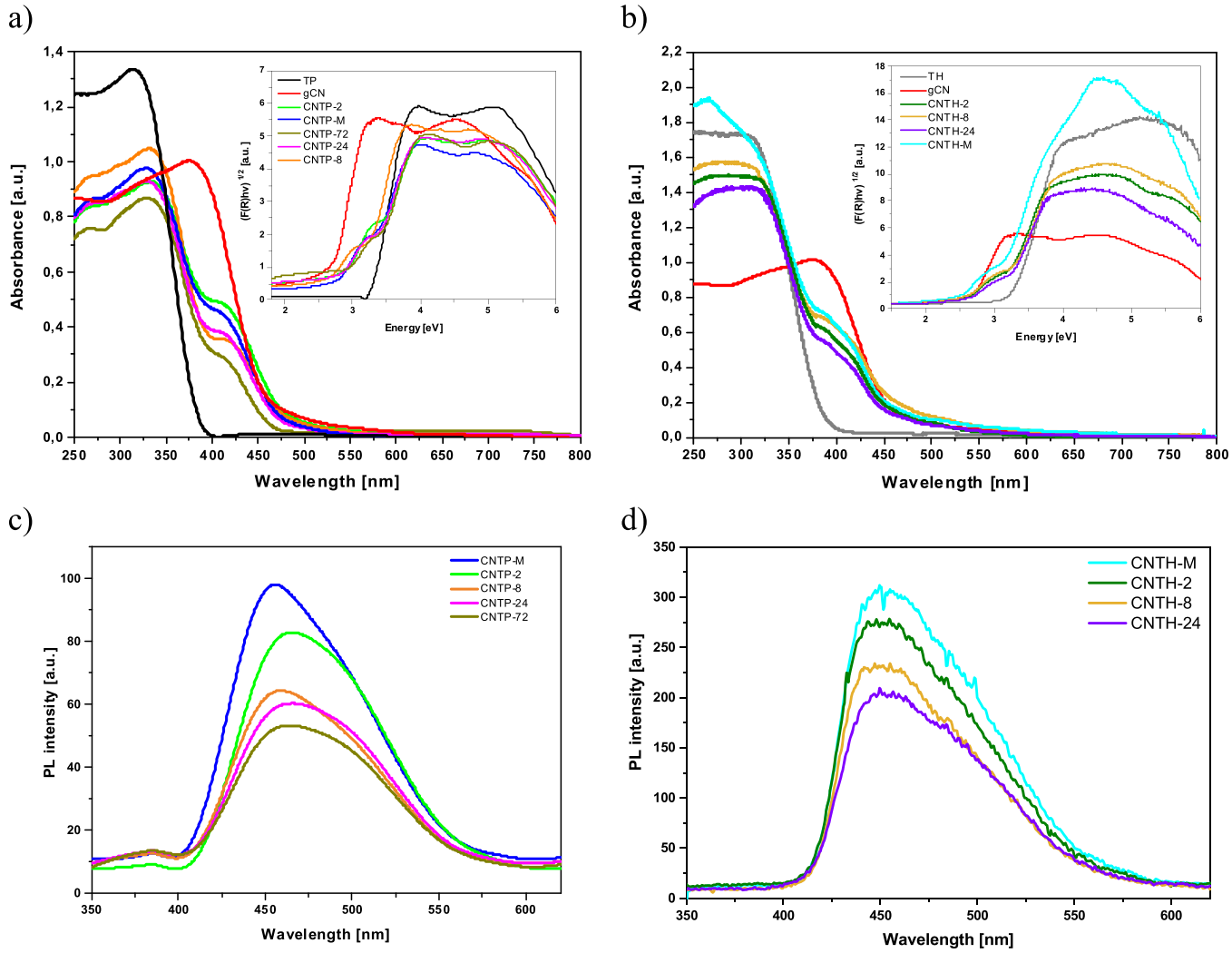

Fig. 5. Results of UV-Vis-DR measurements (inset represents the corresponding Kubelka-Munk curves) and solid photoluminescence (PL) spectra for the CNTP (a, c) and CNTH (b, d) series of samples. The PL measurements were performed with the appropriate settings for g-C_3N_4.

groups [44,45]. Similar to the C 1 s spectra, the N 1 s spectra for mortar and calcined composites also show a very similar shape and position of the main peak, indicating a similar N environment for these samples. O 1 s spectra (Fig. 4) consist of a low binding energy feature at 529.9 eV corresponding to the metal oxides in TiO_2, regardless of the TiO_2 used (either TP or TH). The high binding energy shoulder consists of hydroxides (at 531.4 eV, Fig. S6d) and water molecules remaining on the surface of the samples (at 532.3 eV, Fig. S6d). The O 1 s spectrum for CN shows significantly greater amounts of water compared to other O-containing species. The other samples did not contain significant amounts of water on the surface [46]. The Ti 2p spectra (Fig. 4) show typical spectra for Ti(IV), with the main feature corresponding to Ti $2p_{3/2}$ and a less intense feature corresponding to Ti $2p_{1/2}$ (Fig. S6e). The spectra for all samples show no low binding energy shoulder of the main peak, indicating that Ti(III) was not formed. Although no major differences in binding energies were observed between the different composites, a slight shift of the binding energy peak positions was observed when comparing the pure components to the composites. In the study performed by Gan et al. [47], where they studied a similar g-C_3N_4/TiO_2 system, it is stated that these binding energy shifts indicate that the electrons will migrate from g-C_3N_4 to TiO_2 during the formation of the g-C_3N_4/TiO_2 heterojunction. The charge carrier transfer process will be discussed in more detail in chapter 3.6.

3.3. Optical and electronic properties of the investigated materials

The UV-Vis-DR measurements were performed to determine the light absorption properties of the synthesized materials. The band gap (BG) values of the investigated materials were estimated using the Kubelka-Munk theory (Eq. (1)):

$$(\alpha h\nu)^2 = A(h\nu - E_g) \quad (1)$$

where α, $h\nu$, E_g and A are the absorption coefficient, photon energy, direct band gap and proportional constant.

From the graphs in Fig. 5a and b (Table 2), we can observe that pure CN exhibits light absorption in the visible-light region with a moderate band gap value of 2.61 eV. The visible-light absorption of g-C_3N_4 is enabled due to the charge transfer of the electron from the valence band (VB) of the N 2p orbital to the conduction band (CB) C 2p orbital [16]. In contrast, the BG values of the pure TP and TH samples are 3.28 and 3.26 eV, respectively. From the results of the measurements presented in the previous chapters, we know that the CN, TP and TH components did not change significantly in terms of structure/morphology and chemical composition during the synthesis of g-C_3N_4/TiO_2 composites. Therefore, it is not surprising that all the investigated composites exhibited the ability to absorb light in the visible-light region and that their BG values are in between the

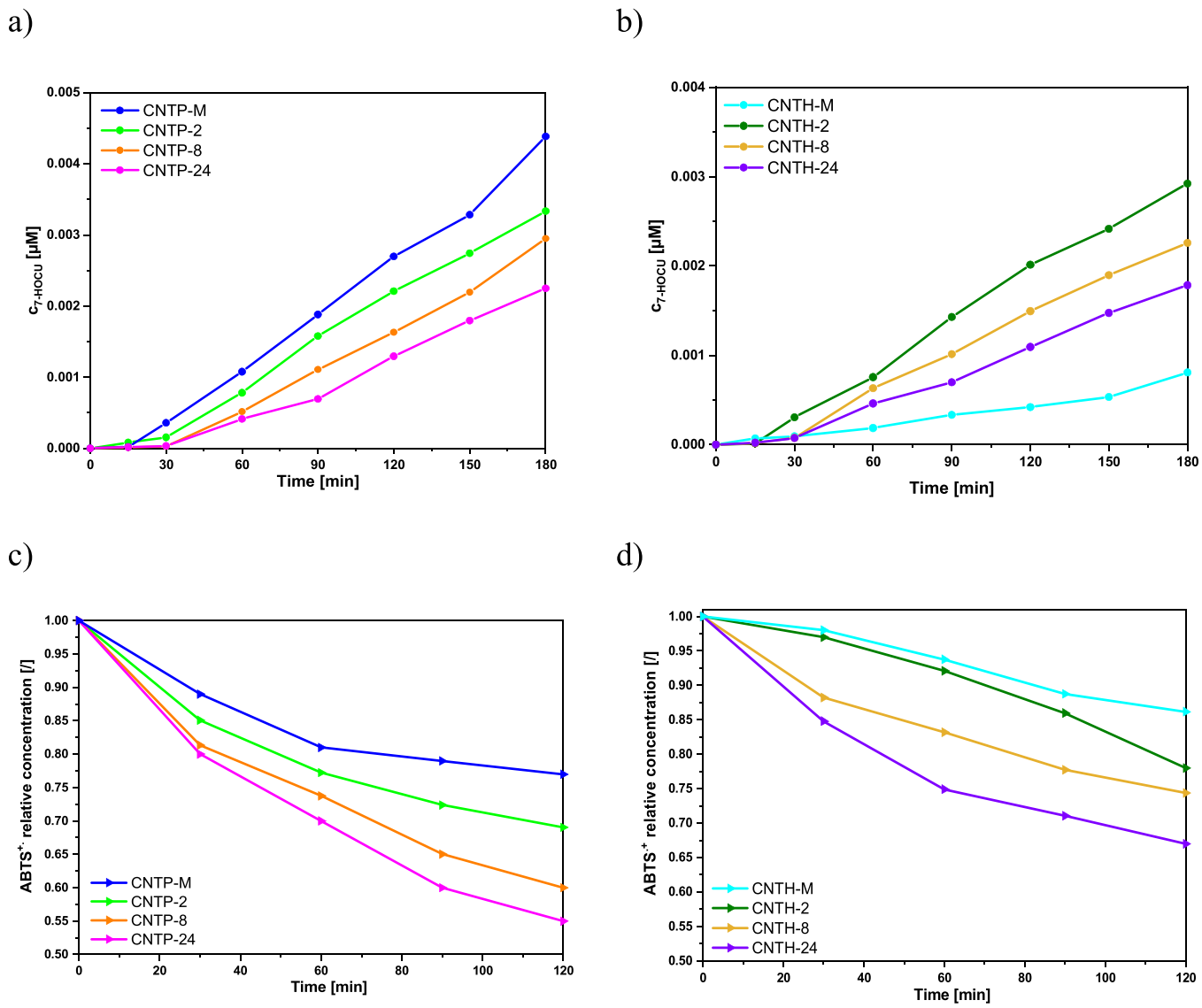

Fig. 6. Concentration of 7-HOCU and ABTS^{+}·relative concentration under visible-light illumination as a function of time for the CNTP (a,c) and CNTH (b,d) series of the investigated photocatalysts.

values of the pure components (Table 2). The BG values of the CNTP-M and CNTH-M samples are thus 3.09 and 2.99 eV, respectively. By prolonging the calcination time, the BG values increase to 3.20 (CNTP-72) and 3.09 eV (CNTH-24) as the CN weight content decreases (Table 2). From Fig. S7a, we can observe that the BG values do not change for the pure CN calcined for different durations compared to its untreated counterpart (Table 2).

From the UV-Vis-DR measurements, we also estimated the edge potentials of the valence band (E_{VB}) and conduction band (E_{CB}) of TP, TH and CN solids using Eqs. (2) and (3):

$$E_{VB} = \chi - E^e + \frac{1}{2}E_g \quad (2)$$

$$E_{CB} = E_{VB} - E_g \quad (3)$$

where E_g is the BG value of CN (2.61 eV), TP (3.28 eV) and TH (3.26 eV), χ is the electronegativity, which has a value of 4.73 eV for g-C_3N_4 and 5.81 eV for TiO_2, and E^e is the energy of free electrons on the hydrogen scale (4.5 eV vs. NHE) [16,18]. Calculations using Eq. (2) revealed that the estimated E_{VB} for CN, TP and TH solids are 1.54, 2.95 and 2.94 eV, respectively. Consequently, the estimated E_{CB} are − 1.08, − 0.33 and − 0.32 eV for the CN, TP and TH samples. From the obtained results, we can confirm that the estimated edge potentials are appropriate for the formation of a heterostructure in both photocatalyst series, which enables the separation of charge carriers generated in the photocatalysts upon visible-light illumination.

To evaluate the tendency of the investigated materials toward the charge carrier recombination process, solid photoluminescence (PL) measurements were performed [48]. All measurements, the results of which are illustrated in Figs. 5c, 5d and S7, were performed using parameters optimal for g-C_3N_4, as TiO_2 requires a lower excitation wavelength due to its high band gap value (comparison for pure TP in Fig. S7c). It can be observed that the pure TP sample exhibited a high charge carrier recombination tendency, which is also observed for the pure CN sample. The calcination for pure CN did not affect its tendency significantly (Fig. S7b). Therefore, the combination of both semiconductors is favourable, as it can decrease the charge carrier recombination tendency (Fig. 5c and d) due to the injection of photogenerated electrons from the CB of CN to the CB of TP/TH [16]. The maximum in PL spectra originates from CN, as g-C_3N_4 materials exhibit the following states: sp^3 C-N σ band, sp^2 C-N π band and the lone pair (LP) state of the bridge nitride atom. This enables three different transitions that occur simultaneously: σ*-LP, π*-LP and π*-π [18,49,50]. The injection of photogenerated electrons from the CB of

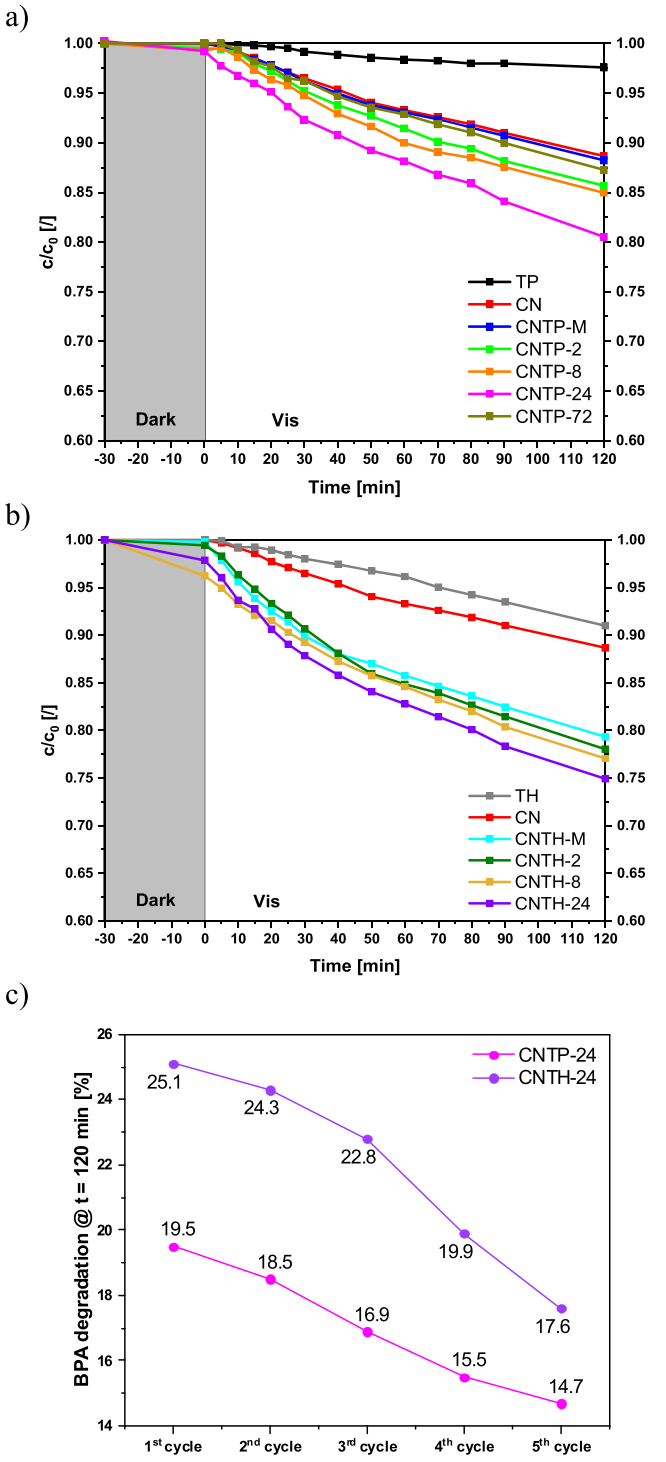

Fig. 7. Photocatalytic degradation of an aqueous solution of BPA (c_0 =10.0 mg/L) conducted at T = 25 °C in the presence of selected photocatalysts (a and b) ($c_{cat.}$=125 mg/L) under visible-light illumination and the results of the reusability tests of the CNTP-24 and CNTH-24 samples for five consecutive cycles (c).

CN into the CB of TP/TH generally decreases the probability of π*-LP and π*-π relaxation emissions in CN (see Supplementary Information for PL deconvolution) [18]. Therefore, all the investigated composites exhibit a prolonged "lifetime" of charge carriers compared to their pure components, as the prolonged calcination time improving the contact between the components enables a more efficient charge carrier separation. These results are also congruent with the analogous EIS measurements (see Supplementary Information).

3.4. Generation of reactive oxygen species

To study the formation of·OH, via either direct or indirect pathway [51,52], scavenger experiments using water-dissolved coumarin as a probe molecule were performed to measure the·OH generation rate via the formation of 7-hydroxycoumarin (7-HOCU). The concentration of generated 7-HOCU by visible-light illumination (the energy spectrum of the light source is shown in Fig. S10a) of the investigated composites was calculated using the calibration curve in Fig. S10c. We can observe that the CNTP-M composite expressed the highest·OH radicals generation rate within the CNTP series (Fig. 6a). On the other hand, the CNTH-M sample exhibited the lowest·OH radicals generation rate in the CNTH series (Fig. 6b). In the case of the CNTH-M sample, the CN component is present in a defined canvas-like form that forms larger aggregates of g-C_3N_4 with corners in every direction and more space between the TH aggregates (see TEM analysis, Fig. 2). A more canvas-like morphology of CN could influence the O_2^- radical formation and its transformation into·OH, which is typical for g-C_3N_4 materials. When the calcination time is increased from 2 to 24 h, the generation of·OH radicals in all series of the investigated composites decreases, which is a little surprising as the composite with the 24 h calcination time expressed the longest "lifetime" of the charger carriers and the most ordered/defined structure of the investigated composites. The decrease could be due to the lower specific surface area and/or higher BG value of the photocatalysts when they are calcined for 24 h. Additionally, the improved contact covered more TP/TH surface, thus influencing the generation of·OH radicals. Considering only the results of the scavenger experiments with coumarin could, therefore, lead us to wrong conclusions as the·OH radicals might not be the dominant ROS species in our investigated system.

To further investigate this dilemma, we performed ROS scavenger experiments using the reduction of water-dissolved 2,2′-azinobis(3-ethylbenzothiazoline-6-sulfonic acid) diammonium salt ($ABTS^{\cdot+}$) to ABTS via photogenerated electrons (e^-) or/and anionic superoxide (O_2^-) radicals under visible-light illumination (energy spectra of the light source in Fig. S10a) [5,52,53]. From the results illustrated in Fig. 6c and d, we can conclude that all the investigated composites exhibit the ability for the generation of O_2^- radicals. Even more, an interesting trend appeared as the activity toward the reduction of $ABTS^{\cdot+}$ increases by prolonging the calcination time. If we compare the samples CNTP-24 and CNTH-24 with the solids CNTP-M and CNTH-M, we can observe that the prolonged calcination time significantly increases the photocatalytic activity of the composites toward the generation of O_2^-under visible-light illumination. The increase of the activity for the 24 h calcined photocatalyst might originate in the increased "lifetime" of charge carriers, which was enabled due to the injection of photogenerated e^- from the CB of CN to the CB of TP/TH (Fig. 5). As indicated by the results of the $ABTS^{\cdot+}$ reduction tests, these e^- can then form O_2^-, which could be primarily generated by the investigated materials [54–56], although we cannot directly compare the concentration of either·OH or O_2^- radicals.

3.5. Tests of photocatalytic activity

The possible wastewater remediation usage of the synthesized photocatalysts was evaluated using photooxidation experiments under visible light using the water-dissolved endocrine disruptor bisphenol A (BPA) as a model pollutant. All the investigated photocatalysts exhibited visible light activity toward the degradation of BPA (the energy spectrum of the light source used is shown in Fig. S10b). The minor activity of pure TP and pure TH samples (Figs. 7a

Table 3
Initial pseudo-first-order photodegradation reaction rate constant, the extent of bisphenol A (BPA) photooxidation after 120 min under visible-light illumination and the results of total organic carbon (TOC) measurements.

Sample	Initial photodegradation reaction rate constant	BPA degradation	TOC removal		
			Measured	Accumulated	True
	10^{-3}/min	%			
CN	1.46	11.4	8.6	0.8	7.8
TP	0.25	2.4	0.9	0.2	0.7
CNTP-M	1.79	11.8	10.1	1.4	8.7
CNTP-2	2.07	14.3	13.2	1.9	11.3
CNTP-8	2.19	15.0	14.7	1.7	13.0
CNTP-24	2.23	19.5	19.2	1.7	17.5
CNTP-72	1.53	12.7	11.3	1.9	9.4
TH	0.66	9.0	3.2	0.6	2.6
CNTH-M	2.45	20.7	18.4	0.8	17.6
CNTH-2	2.99	22.0	21.4	2.1	19.3
CNTH-8	3.08	23.0	22.1	2.2	19.9
CNTH-24	3.34	25.1	24.8	2.5	22.3

and 7b) can be explained through some surface defects due to the manufacturers' processes. All the investigated composites exhibit higher BPA degradation activity than pure components. These results further show that only minor BPA adsorption onto the catalyst surface occurred during the 30 min dark period, which was used to establish the sorption equilibrium. From the results in Table 3, we can conclude that by increasing the calcination time from 2 to 24 h, the BPA degradation rate increases in both series of the investigated composites. The highest BPA degradation of the 24 h calcined composite occurred due to the improved contact between the components, which resulted in the improvement of the charge carrier separation and the better utilization of the charge carriers for the formation of ROS (O_2^-). The improved separation dynamics were found to be the key factor in increasing the photocatalytic activity and is congruent with the results of analogous systems in literature [16,18,23]. When the calcination time increases to 72 h, the photocatalytic activity of the CNTP composites drops as the lower weight content of g-C_3N_4 increases the BG value of the composite and limits its photocatalytic activity under visible-light illumination. To measure the efficiency of BPA mineralization, we also performed the total organic carbon (TOC) analysis of fresh and treated BPA aqueous solutions (Table 3). Based on the results in Table S3, the carbon accumulation on the surface of the materials during the photooxidation experiments can also be obtained, which was then used to correct the measured TOC values. The obtained data represents the real TOC values, from which we can conclude that the BPA photooxidation occurs with a high degree of mineralization and only a minor accumulation of BPA and/or BPA degradation products onto the surface of the photocatalyst.

The photocatalyst with the highest initial photodegradation reaction rate is CNTH-24, which also exhibited the highest BPA degradation after 120 min of visible-light illumination (25.1%). The high photocatalytic activity of the CNTH series of samples arises from: (i) higher specific surface area (Table 2), (ii) the existence of mesopores in the CNTH samples (Fig. S2d), and (iii) lower BG values (Table 2). In addition, the morphology of the TH compound enabled more profound improvement in the interactions between the components, which is expressed in the steady decrease of the PL emissions (Table S6) as better contact between the components was enabled. The improved activity of the CNTH-24 sample could also be attributed to the higher TiO_2 (in comparison to CNTP-24) and g-C_3N_4 crystallite size, as large crystallite size was favourable for the charge carrier separation and utilization of photogenerated h^+ [23,57]. Additionally, the composites of the CNTH series usually have a slightly more negative zeta potential at the pH value of BPA solution (i.e. 6.17) than the CNTP series, forming a slightly more stable suspension [58]. All these minor and major improvements of the CNTH series compared to the CNTP series contributed to the highest photocatalytic activity of the CNTH-24 sample among all the investigated solids.

In the past, different authors [59,60] have raised concerns about the typical evaluation of photocatalytic activity at equal catalyst concentration (mass of the catalyst) in the reactor system, as the rate of the photocatalytic reaction depends on the total radiant energy absorbed by the catalyst in suspension. Žerjav et al. [61] reported that a photocatalyst with a small average particle size exhibited a higher intensity of turbidity of the catalyst/model molecule aqueous suspension, so the penetration of light irradiation in a batch slurry reactor was hindered, which in turn resulted in the decrease of efficiency of the heterogeneous photocatalytic system. Taking into consideration the "shielding/shadowing" effect, the measured activity of CNTP-8 and CNTP-24 samples should be lower compared to the activity of CNTP-M and CNTP-2 solids, because, based on the average particle size values listed in Table S1, the number of catalyst particles is about three times higher in the former case. However, the opposite was observed in our case (Fig. 7a), i.e. increased photocatalytic activity of investigated nanosolids with smaller average particle sizes. This means that despite the presence of the "shielding/shadowing" effect, we were able to demonstrate that the nature of the interface between phases influences the behaviour of examined catalysts.

We also performed the reusability tests for five consecutive runs using the same catalyst batch (CNTP-24 and CNTH-24). From the results illustrated in Fig. 7c, we observe a decrease in the BPA photooxidation rate with the increasing number of photooxidation runs. In the case of the CNTP-24 sample, we observe a decrease in the photocatalytic activity from 19.5% to 14.7% of BPA conversion at t = 120 min. For the CNTH-24 sample, a slightly larger decrease in the photocatalytic activity toward the BPA conversion from 25.1% to 17.6% was observed. In both cases, the decrease in the photocatalytic activity is probably due to the carbon deposition on the surface of the photocatalysts, which blocks access to the active sites. This blockage was observed to have a higher effect in the case of CNTH-24, probably due to the higher specific surface area and consequently higher accumulated (2.5 wt% C) carbon, thus blocking the access of BPA to h^+.

3.6. The mechanism of the photoexcitation and photooxidation of BPA

From the literature [16,33,62] and the results of the UV-Vis-DR and solid PL measurements (Fig. 5), we propose the charge carrier generation and separation mechanism presented in Fig. 8. Under visible-light illumination, g-C_3N_4 (CN) generates e^- that jump to the CB of g-C_3N_4; the photogenerated h^+ remain in the VB of g-C_3N_4.

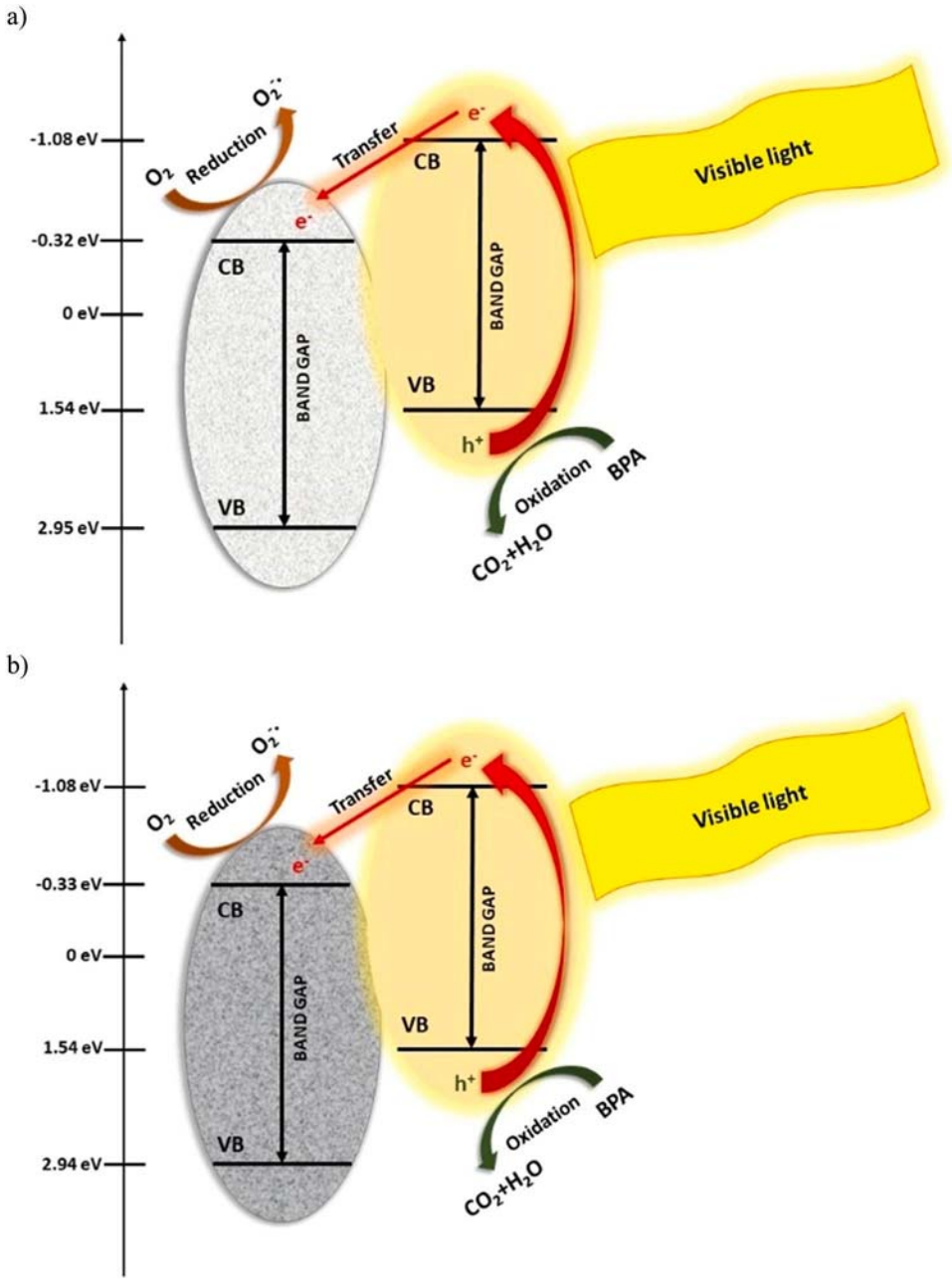

Fig. 8. Purposed photocatalytic mechanism based on the UV-Vis-DR and solid photoluminescence measurements for the CNTP (a) and CNTH (b) composite photocatalysts under visible-light illumination.

Neither TiO_2 components generate charge carriers due to their BG gap value of 3.28 eV (TP) and 3.26 eV (TH). When we combine the components to form a heterostructured composite photocatalyst, the generated e^- in CB of CN can transfer to the CB of TP or TH, whereas the photogenerated h^+ remains in the VB of CN. This is possible due to the formed heterostructure and the favourable, more negative E_{CB} of CN (−1.08 eV vs. NHE) in comparison to E_{CB} TP (−0.32 eV vs. NHE) or TH (−0.33 eV vs. NHE).

The results are also confirmed by the slight shifts of the binding energies in the XPS spectra of the composites (Fig. 4) compared to pure components, which could indicate that the photogenerated electrons in CN will probably migrate to TP/TH [47]. This separation prolongs the "lifetime" of the charge carriers, as seen in a lower solid PL maximum and R_{CT} (Table 2) values for the composites. The E_{CB} of all components are more negative than the reduction potential of oxygen (−0.046 eV vs. NHE) [63], which enables the utilization of migrated e^- to react with water-dissolved oxygen and to generate $O_2^{\cdot-}$. The potential for the·OH/H_2O (2.68 eV vs. NHE) and·OH/$^-$OH (1.99 vs. NHE) [64–66] is too positive for the photogenerated h^+ in VB of CN (E_{VB}=1.54 eV vs. NHE) to produce·OH radicals. Therefore, the photogenerated holes probably directly attack the water-dissolved (and adsorbed) BPA. The suggested type-II heterojunction behaviour is also supported by the results of theoretical studies performed by other research groups [67].

To confirm these findings, several quenching experiments were performed (Fig. S11c and d). The addition of BQ ($O_2^{\cdot-}$), NaN_3 ($^1O_2$), MeOH (·OH) and HCOOH (h^+) can have an impact on the photooxidation rate of BPA, depending on which species are responsible for its degradation under visible-light illumination. The photooxidation of BPA conducted in the presence of the CNTP-24 or CNTH-24 sample is not affected significantly by the addition of NaN_3 or MeOH. Therefore, $^1O_2$ and·OH are not the dominant ROS responsible

for the BPA degradation. The addition of HCOOH minor decreases the photocatalytic activity of the CNTP-24 sample and, more significantly, decreases for the CNTH-24. The reason could originate in the higher specific surface area of the CNTH-24, which benefits the utilization of h^+. When BQ is added to the reaction mixture, BPA degradation is practically non-existent in both investigated photocatalysts. Therefore, the major ROS involved in the photooxidation of BPA under visible-light illumination are O_2^-, as expected from the results of the ROS scavenger experiments and h^+, although their utilization is probably limited due to the lower specific surface area of the CNTP-24 sample. These findings are also consistent with the results for analogous systems found in the literature [54–56,68–71] and provide additional information about the process of heterogeneous photocatalytic oxidation and enable the better optimization of photocatalyst synthesis in the future.

4. Conclusions

In the present study, we successfully synthesized pure g-C_3N_4 material by simple thermal treatment of dicyandiamide at 550 °C. Using a simple mortar synthesis method, we combined g-C3N4 (CN) with one of the two commercially available TiO_2 (TP /TH). To examine the effect of g-C_3N_4 "melting" on the photocatalytic activity of the prepared g-C_3N_4/TiO_2 composites, the mortar synthesis method was extended by a final calcination step at 350 °C in the air for 2, 8, 24 or 72 h. Based on the structural and textural characterization results, we found no (or only minor) changes in the chemical and structural properties of the two components. However, we found evidence that increasing the calcination time improved the contact area between g-C_3N_4 and TiO_2, regardless of which TiO_2 was used. The improvement of the junction was possible due to the relative thermal (in)stability of g-C_3N_4, which acted as a binder ("cheese") to bond the TiO_2 nanoparticles together. This is also evident from the elemental analysis results, where a prolonged calcination time decreased the amount of g-C_3N_4 in the studied composites. The addition of g-C_3N_4 allowed the composites to absorb and utilize visible light, as the CN component has a moderate BG value of 2.61 eV. As the duration of calcination increased, the BG values of the studied composites increased as the g-C_3N_4 material decomposed. Therefore, choosing a suitable calcination duration allows BG tailoring of the composites. Based on the suitable energy of the edge potentials of CB and VB for both components, a heterostructured composite photocatalyst was formed, which allowed the injection of photogenerated e^- from the CB of CN to the CB of TP/TH. From the results of solid PL and EIS measurements of the prepared materials, we can conclude that the improved contact between the components positively affected the injection of photogenerated e^- as the intensity of the PL signal and the value of the R_{CT} decreased. The improved charge carrier separation and the resulting extension of the charge carrier "lifetime" led to the better utilization of the photogenerated e^- and h^+. This was confirmed by the results of the ROS scavenger and BPA photooxidation experiments under visible-light illumination. All the composites studied showed a high degree of BPA mineralization. The highest photocatalytic activity under visible-light illumination was exhibited by the CNTP-24 and CNTH-24 samples. The calcination time of 24 h optimally improved the contact area between the components, improving the charge carrier separation, which was found to be a rate-limiting step for increasing the photocatalytic activity. The CNTH-24 photocatalyst exhibited the greatest activity in the degradation of BPA. The component TH increased the interaction between CN and TH, thus improving the utilization of charge carriers compared to the component TP. In addition, the CNTH samples exhibited higher specific surface area and more negative zeta potential. This means that the photogenerated h^+ and ROS had easier access to the BPA molecules, and the catalyst/BPA water suspension was stabilized. The results of experiments using different charge carrier scavengers showed that the species involved in the photooxidation of BPA under visible-light illumination are O_2^- and h^+. The results of this work provide new insights into the synthesis conditions of g-C_3N_4/TiO_2-based photocatalysts and show how their potential for wastewater treatment under visible-light illumination can be enhanced.

CRediT authorship contribution statement

Matevž Roškarič: Investigation, Validation. **Gregor Žerjav**: Conceptualization, Investigation, Validation, Writing – original draft, Visualization, Supervision. **Matjaž Finšgar:** Investigation, Visualization. **Janez Zavašnik:** Investigation, Visualization. **Albin Pintar:** Writing – review & editing, Funding acquisition.

Data availability

Data will be made available on request.

Declaration of Competing Interest

The authors declare that they have no known competing financial interests or personal relationships that could have appeared to influence the work reported in this paper.

Acknowledgements

The authors acknowledge the financial support from the Slovenian Research Agency (research core funding no. P2–0150, P1–0417, P2–0118). Acknowledgements also go the CristalACTIiV™ company for their generous donation of a commercially available TiO_2 powder DT-51. The project is co-financed by the Republic of Slovenia, the Ministry of Education, Science and Sport and the European Union under the European Regional Development Fund.

Appendix A. Supporting information

Supplementary data associated with this article can be found in the online version at doi:10.1016/j.jallcom.2023.169585.

References

[1] M. Ismael, Environmental remediation and sustainable energy generation via photocatalytic technology using rare earth metals modified g-C_3N_4: A review, J. Alloy. Compd. 931 (2023) 167469, https://doi.org/10.1016/j.jallcom.2022.167469
[2] M. Ismael, A review on graphitic carbon nitride (g-C_3N_4) based nanocomposites: Synthesis, categories, and their application in photocatalysis, J. Alloy. Compd. 846 (2020) 156446, https://doi.org/10.1016/j.jallcom.2020.156446
[3] R. Kaplan, B. Erjavec, A. Pintar, Enhanced photocatalytic activity of single-phase, nanocomposite and physically mixed TiO_2 polymorphs, Appl. Catal. A 489 (2015) 51–60, https://doi.org/10.1016/j.apcata.2014.10.018
[4] G. Žerjav, A. Pintar, M. Ferentz, M. Landau, A. Haimovich, A. Goldbourt, M. Herskowitz, Effect of surface chemistry and crystallographic parameters of TiO_2 anatase nanocrystals on photocatalytic degradation of bisphenol A, Catalysts 9 (2019) 447, https://doi.org/10.3390/catal9050447
[5] G. Žerjav, J. Zavašnik, J. Kovač, A. Pintar, The influence of Schottky barrier height onto visible-light triggered photocatalytic activity of TiO_2 + Au composites, Appl. Surf. Sci. 543 (2021) 148799, https://doi.org/10.1016/j.apsusc.2020.148799
[6] N.F.F. Moreira, M.J. Sampaio, A.R. Ribeiro, C.G. Silva, J.L. Faria, A.M.T. Silva, Metal-free g-C_3N_4 photocatalysis of organic micropollutants in urban wastewater under visible light, Appl. Catal. B 248 (2019) 184–192, https://doi.org/10.1016/j.apcatb.2019.02.001
[7] G. Žerjav, M. Roškarič, J. Zavašnik, J. Kovač, A. Pintar, Effect of Au Loading on Schottky barrier height in TiO_2 + Au plasmonic photocatalysts, Appl. Surf. Sci. 549 (2022) 152196, https://doi.org/10.1016/j.apsusc.2021.152196
[8] G. Žerjav, A. Pintar, Influence of TiO_2 Morphology and Crystallinity on Visible-Light Photocatalytic Activity of TiO_2-Bi_2O_3 Composite in AOPs, Catalysts 10 (2020) 395, https://doi.org/10.3390/catal10040395
[9] G. Žerjav, G. Scandura, C. Garlisi, G. Palmisano, A. Pintar, Sputtered vs. sol-gel TiO_2-doped films: Characterization and assessment of aqueous bisphenol A oxidation under UV and visible light radiation, Catal. Today 357 (2020) 380–391, https://doi.org/10.1016/j.cattod.2019.09.027

[10] M. Roškarič, G. Žerjav, J. Zavašnik, A. Pintar, The influence of synthesis conditions on the visible-light triggered photocatalytic activity of g-C_3N_4/TiO_2 composites used in AOPs, J. Environ. Chem. Eng. 10 (2022) 107656, https://doi.org/10.1016/j.jece.2022.107656

[11] A. Son, J. Lee, M.G. Seid, E. Rahman, J. Choe, K. Cho, J. Lee, S.W. Hong, Ti^{3+} self-doped TiO_2 nanotube arrays revisited as Janus photoelectrodes for persulfate activation and water treatment, Appl. Catal. B 315 (2022) 121543, https://doi.org/10.1016/j.apcatb.2022.121543

[12] M.R. Rajeshwari, S. Kokilavani, S.S. Khan, Recent developments in architecturing the g-C_3N_4 based nanostructured photocatalysts: Synthesis, modifications and applications in water treatment, Chemosphere 291 (2022) 132735, https://doi.org/10.1016/j.chemosphere.2021.132735

[13] S. Cao, J. Yu, g-C_3N_4-based photocatalysts for hydrogen generation, J. Phys. Chem. Lett. 5 (2014) 2101–2107, https://doi.org/10.1021/jz500546b

[14] S.B. Vuggili, U.K. Gaur, M. Sharma, 2D/2D facial interaction of nitrogen-doped g-C_3N_4/In_2S_3 nanosheets for high performance by visible-light-induced photocatalysis, J. Alloy. Compd. 902 (2022) 163757, https://doi.org/10.1016/j.jallcom.2022.163757

[15] C. Xing, G. Yu, J. Zhpu, Q. Liu, T. Chen, H. Liu, X. Li, Solar energy-driven upcycling of plastic waste on direct Z-scheme heterostructure of V-substituted phosphomolybdic acid/g-C_3N_4 nanosheets, Appl. Catal. B 315 (2022) 121496, https://doi.org/10.1016/j.apcatb.2022.121496

[16] R. Hao, G. Wang, H. Tang, L. Sun, C. Xu, D. Han, Template-free preparation of macro/mesoporous g-C_3N_4/TiO_2 heterojunction photocatalysts with enhanced visible light photocatalytic activity, Appl. Catal. B 187 (2016) 47–58, https://doi.org/10.1016/j.apcatb.2016.01.026

[17] A.T. Sareshkeh, R.B. Some-Saraee, M.H. Rasoulifard, M.-S. Seyed-Dorraji, S.F. Hosseini, P and C co-modified g-C_3N_4/SiO_2/ZnO Z-scheme based heterogeneous nanocomposite as a highly boosted visible-light-driven photocatalytic system, J. Alloy. Compd. 923 (2022) 166392, https://doi.org/10.1016/j.jallcom.2022.166392

[18] K. Kočí, M. Reli, I. Troppová, M. Šihor, J. Kupková, P. Kustrowski, P. Praus, Photocatalytic decomposition of N_2O over TiO_2/g-C_3N_4 photocatalysts heterojunction, Appl. Surf. Sci. 396 (2017) 1685–1695, https://doi.org/10.1016/j.apsusc.2016.11.242

[19] S. Dong, S. Chen, F. He, J. Li, H. Li, K. Xu, Construction of a novel N-doped oxygen vacancy-rich TiO_2 N-TiO_{2-x}/g-C_3N_4 S-scheme heterostructure for visible light driven photocatalytic degradation of 2,4-dinitrophenylhydrazine, J. Alloy. Compd. 908 (2022) 164586, https://doi.org/10.1016/j.jallcom.2022.164586

[20] K. Abderrazek, F.S. Najoua, E. Srasra, Synthesis and characterization of [Zn-Al] LDH: Study of the effect of calcination on the photocatalytic activity, Appl. Clay Sci. 119 (2016) 229–235, https://doi.org/10.1016/j.clay.2015.10.014

[21] Y. Fan, M. Deng, G. Chen, Q. Zhang, Y. Luo, D. Li, Q. Meng, Effect of calcination on the photocatalytic performance of CdS under visible light irradiation, J. Alloy. Compd. 509 (2011) 1477–1481, https://doi.org/10.1016/j.jallcom.2010.10.044

[22] C. Li, X. Liu, X. Yang, T. Peng, Y. Li, M. Chen, C. Lin, J. Jiang, Z. Su, W. Kong, Y. Wang, Tetragonal multilayered ZnO/CuO composites derived from Zn- and Cu-containing metal-organic framework: Effect of calcination temperature on physicochemical properties and photocatalytic activity, Ceram. Int. 48 (2022) 18460–18467, https://doi.org/10.1016/j.ceramint.2022.03.115

[23] M. Reli, K. Kočí, V. Matějka, P. Kovár, L. Obalová, Effect of calcination temperature and calcination time on the kaolinite/TiO_2 composite for photocatalytic reduction of CO_2, GeoSci. Eng. LVIII (2012) 10–22, https://doi.org/10.2478/v10205-011-0022-2

[24] E.S.M. Mouele, M. Dinu, F. Cummings, O.O. Fatoba, M.T.Z. Myint, H.H. Kyaw, A.C. Parau, A. Vladescu, M.G. Francesconi, S. Pescetelli, A.D. Carlo, A. Agresti, M. Al-Abri, S. Dobretsov, M. Braic, L.F. Petrik, Effect of calcination time on the physicochemical properties and photocatalytic performance of carbon and nitrogen co-doped TiO_2 nanoparticles, Catalysts 10 (2020) 847, https://doi.org/10.3390/catal10080847

[25] W. Zhang, H. Xin, R. Li, H. He, Effects of calcination time on structure and activity of porous TiO_2-Al_2O_3 photocatalyst, Asian J. Chem. 25 (2013) 3769–3772, https://doi.org/10.14233/ajchem.2013.13758

[26] Y. Yan, M. Yang, C. Wang, E. Liu, X. Hu, J. Fan, Defected ZnS/bulk g-C_3N_4 heterojunction with enhanced photocatalytic activity for dyes oxidation and Cr (VI) reduction, Colloids Surf. A Physicochem. Eng. Asp. 582 (2019) 123861, https://doi.org/10.1016/j.colsurfa.2019.123861

[27] H. Yan, Z. Zhu, Y. Long, W. Li, Single-source-precursor-assisted synthesis of porous WO_3/g-C_3N_4 with enhanced photocatalytic property, Colloids Surf. A Physicochem. Eng. Asp. 582 (2019) 123857, https://doi.org/10.1016/j.colsurfa.2019.123857

[28] Shimadzu, FTIR Analysis Q&A, Can you tell me why the spectrum baseline is curved?, https://www.shimadzu.com/an/service-support/faq/ftir/5/index.html, (Accessed 25 May 2022).

[29] H. Zhang, F. Liu, H. Wu, X. Cao, J. Sun, W. Lei, *In situ* synthesis of g-C_3N_4/TiO_2 heterostructures with enhanced photocatalytic hydrogen evolution under visible light, RSC Adv. 7 (2017) 40327–40333, https://doi.org/10.1039/C7RA06786K

[30] J. Wang, S. Yin, Q. Zhang, F. Cao, Y. Xing, Q. Zhao, Y. Wang, W. Xu, W. Wu, M. Wu, Single-Atom Fe-N_4 sites promote the triplet-energy transfer process of g-C_3N_4 for the photooxidation, J. Catal. 404 (2021) 89–95, https://doi.org/10.1016/j.jcat.2021.09.010

[31] H. Sun, C. Zou, Y. Liao, W. Tang, Y. Huang, M. Chen, Modulating charge transport behaviour across the interface via g-C_3N_4 surface discrete modified BiOI and Bi_2MoO_6 for efficient photodegradation of glyphosate, J. Alloy. Compd. 935 (Part 1) (2023) 168208, , https://doi.org/10.1016/j.jallcom.2022.168208

[32] Z. Li, X. Meng, Z. Zhang, Fabrication of surface hydroxyl modified g-C_3N_4 with enhanced photocatalytic oxidation activity, Catal. Sci. Technol. 9 (2019) 3979–3993, https://doi.org/10.1039/C9CY00550A

[33] L. Ma, G. Wang, C. Jiang, H. Bao, Q. Xu, Synthesis of core-shell TiO_2@g-C_3N_4 hollow microspheres for efficient photocatalytic degradation of rhodamine B under visible light, Appl. Surf. Sci. 430 (2018) 263–272, https://doi.org/10.1016/j.apsusc.2017.07.282

[34] J. Feng, K. Xie, Q. Kang, Y. Gou, Facile fabrication of g-C_3N_4/CdS heterojunctions with enhanced visible-light photocatalytic degradation performances, J. Sci.: Adv. Mater. Dev. 7 (2022) 100409, https://doi.org/10.1016/j.jsamd.2021.100409

[35] J. Li, M. Zhang, Q. Li, J. Yang, Enhanced visible light activity on direct contact Z-scheme g-C_3N_4-TiO_2 photocatalyst, Appl. Surf. Sci. 391 (2017) 184–193, https://doi.org/10.1016/j.apsusc.2016.06.145

[36] Md.M. Rahman, A.Z. Shafiullah, A. Pal, I. Md.A. Islam, B.B. Jahan, Saha, Study on Optimum IUPAC adsorption isotherm models employing sensitivity of parameters for rigorous adsorption system performance evaluation, Energies 14 (2021) 7478, https://doi.org/10.3390/en14227478

[37] K.A. Cychosz, M. Thommes, Progress in the physisorption characterization of nanoporous gas storage materials, Engineering 4 (2018) 559–566, https://doi.org/10.1016/j.eng.2018.06.001

[38] L. Palmisano, V. Augugliaro, M. Schiavello, A. Sclafani, Influence of acid-base properties on photocatalytic and photochemical processes, J. Mol. Catal. 56 (1989) 284–295, https://doi.org/10.1016/0304-5102(89)80192-0

[39] C. Bellmann, A. Caspari, C. Moitzi, F. Babick, M. Schäffler, T. Luxbacher, M. Stintz, Dynamic and electrophoretic light scattering: guidelines for particle size analysis and zeta potential determination, Anton Paar GmbH, Austra (2019).

[40] B. Zhu, P. Xia, W. Ho, J. Yu, Isoelectric point and adsorption activity of porous g-C_3N_4, Appl. Surf. Sci. 344 (2015) 188–195, https://doi.org/10.1016/j.apsusc.2015.03.086

[41] Y. Li, M.-Q. Wang, S.-J. Bao, S. Lu, M. Xu, D. Long, S. Pu, Tuning and thermal exfoliation graphene-like carbon nitride nanosheets for superior photocatalytic activity, Ceram. Int. 42 (2016) 18521–18528, https://doi.org/10.1016/j.ceramint.2016.08.190

[42] I. Papailias, N. Todorova, T. Giannakopoulou, N. Ioannidis, N. Boukos, C.P. Athanasekou, D. Dimotikali, C. Trapalis, Chemical vs thermal exfoliation of g-C_3N_4 for NO_x removal under visible light irradiation, Appl. Catal. B 239 (2018) 16–26, https://doi.org/10.1016/j.apcatb.2018.07.078

[43] F. Dong, Y. Li, Z. Wang, W.-K. Ho, Enhanced visible light photocatalytic activity and oxidation ability of porous graphene-like g-C_3N_4 nanosheets via thermal exfoliation, Appl. Surf. Sci. 358 (2015) 393–403, https://doi.org/10.1016/j.apsusc.2015.04.034

[44] Q. Guo, Y. Xie, X. Wang, S. Lv, T. Hou, X. Liu, Characterization of well-crystallized graphitic carbon nitride nanocrystallites via a benzene-thermal route at low temperatures, Chem. Phys. Lett. 380 (2003) 84–87, https://doi.org/10.1016/j.cplett.2003.09.009

[45] X. Zhang, X.R. Zhang, P. Yang, H.-S. Chen, S.P. Jiang, Black magnetic Cu-g-C_3N_4 nanosheets towards efficient photocatalytic H_2 generation and CO_2/benzene conversion, Chem. Eng. J. 450 (2022) 138030, https://doi.org/10.1016/j.cej.2022.138030

[46] L. Wang, X. Fei, L. Zhang, J. Yu, B. Cheng, Y. Ma, Solar fuel generation over nature-inspired recyclable TiO_2/g-C_3N_4 S-scheme hierarchical thin-film photocatalyst, J. Mater. Sci. Technol. 112 (2022) 1–10, https://doi.org/10.1016/j.jmst.2021.10.016

[47] W. Gan, X. Fu, J. Guo, M. Zhang, D. Li, C. Ding, Y. Lu, P. Wang, Z. Sun, Ag nanoparticles decorated 2D/2D TiO_2/g-C_3N_4 heterojunction for efficient removal of tetracycline hydrochloride: Synthesis, degradation pathways and mechanism, Appl. Surf. Sci. 606 (2022) 154837, https://doi.org/10.1016/j.apsusc.2022.154837

[48] S. Yang, H. Li, H. Li, W. Qi, Q. Zhang, J. Zhu, P. Zhao, L. Chen, Rational design of 3D carbon nitrides assemblies with tunable nano-building blocks for efficient visible-light photocatalytic CO_2 conversion, Appl. Catal. B 316 (2022) 121612, , https://doi.org/10.1016/j.apcatb.2022.121612

[49] D. Das, S.L. Shinde, K.K. Nanda, Temperature-Dependent Photoluminescence of g-C_3N_4: Implication for Temperature Sensing, ACS Appl. Mater. Interfaces 8 (2016) 2181–2186, https://doi.org/10.1021/acsami.5b10770

[50] C. Hu, W.-Z. Hung, M.-S. Wang, P.-J. Lu, Phosphorus and sulfur codoped g-C_3N_4 as an efficient metal-free photocatalyst, Carbon 127 (2018) 374–383, https://doi.org/10.1016/j.carbon.2017.11.019

[51] G. Žerjav, A. Albreht, I. Vovk, A. Pintar, Revisiting terephthalic acid and coumarin as probes for photoluminescent determination of hydroxyl radical formation rate in heterogenous photocatalysis, Appl. Catal. A 598 (2020) 117566, https://doi.org/10.1016/j.apcata.2020.117566

[52] A. Houas, H. Lachheb, M. Ksibi, E. Elaloui, C. Guillard, J.-M. Herrmann, Photocatalytic degradation pathway of methylene blue in water, Appl. Catal. B 31 (2001) 145–157, https://doi.org/10.1016/S0926-3373(00)00276-9

[53] P.J. Collins, A.D.W. Dobson, J.A. Field, Reduction of the 2,2′-Azinobis(3-Ethylbenzthiazoline-6-Sulfonate) Cation Radical by Physiological Organic Acids in the Absence and Presence of Manganese, ASM Appl. Environ. Microbiol 64 (1998), pp. 2026–2031, https://doi.org/10.1128/AEM.64.6.2026-2031.1998

[54] S. Luan, D. Qu, L. An, W. Jiang, X. Gao, S. Hua, X. Miao, Y. Wen, Z. Sun, Enhancing photocatalytic performance by constructing ultrafine TiO_2 nanorods/g-C_3N_4 nanosheets heterojunction for water treatment, Sci. Bull. 63 (2018) 683–690, https://doi.org/10.1016/j.scib.2018.04.002

[55] H. Wang, Q. Li, S. Zhang, Z. Chen, W. Wang, G. Zhao, L. Zhuang, B. Hu, X. Wang, Visible-light-driven N_2-g-C_3N_4 as a highly stable and efficient photocatalyst for bisphenol A and Cr(VI) removal in binary systems, Catal. Today 335 (2019) 110–116, https://doi.org/10.1016/j.cattod.2018.09.037

[56] W. He, Y. Wang, C. Fan, Y. Wang, X. Zhang, J. Liu, R. Li, Enhanced charge separation and increased oxygen vacancies of h-BN/OV-BiOCl for improved visible-light photocatalytic performance, RSC Adv. 9 (2019) 14286–14295, https://doi.org/10.1039/c9ra01639b

[57] C.B. Almquist, P. Biswas, Role of synthesis method and particle size of nanostructured TiO_2 on its photoactivity, J. Catal. 212 (2002) 145–156, https://doi.org/10.1006/jcat.2002.3783

[58] R. Garg, R. Gupta, A. Bansal, Degradation mechanism, reaction pathways and kinetics for the mineralization of Bisphenol A using hybrid ZnO/graphene oxide nano-catalysts, Korean J. Chem. Eng. 38 (2021) 485–497, https://doi.org/10.1007/s11814-020-0718-8

[59] R. Acosta-Herazo, M.Á. Mueses, Fi Machuca-Martínez, G. Li Puma, Impact of photocatalyst optical properties on the efficiency of solar photocatalytic reactors rationalized by the concepts of initial rate of photon absorption (IRPA) dimensionless boundary layer of photon absorption and apparent optical thickness, Chem. Eng. J. 356 (2019) 839–849, https://doi.org/10.1016/j.cej.2018.09.085

[60] D. Dolat, N. Quici, E. Kusiak-Nejman, A.W. Morawski, G. Li Puma, One-step, hydrothermal synthesis of nitrogen, carbon co-doped titanium dioxide (N,C TiO_2) photocatalysts. Effect of alcohol degree and chain length as carbon dopant precursors on photocatalytic activity and catalyst deactivation, Appl. Catal. B 115–116 (2012) 81–89, https://doi.org/10.1016/j.apcatb.2011.12.007

[61] G. Žerjav, K. Žižek, J. Zavašnik, A. Pintar, Brookite vs. rutile vs. anatase: What`s behind their various photocatalytic activities? J. Environ. Chem. Eng. 10 (2022) 107722, https://doi.org/10.1016/j.jece.2022.107722

[62] B. Liu, M. Qiao, Y. Wang, L. Wang, Y. Gong, T. Huo, X. Zhao, Persulfate enhanced photocatalytic degradation of bisphenol A by g-C_3N_4 nanosheets under visible light irradiation, Chemosphere 189 (2017) 115–122, https://doi.org/10.1016/j.chemosphere.2017.08.169

[63] B. Chai, T. Peng, J. Mao, K. Li, L. Zan, Graphitic carbon nitride (g-C_3N_4)-Pt-TiO_2 nanocomposite as an efficient photocatalyst for hydrogen production under visible light irradiation, Phys. Chem. Chem. Phys. 14 (2012) 16745–16752, https://doi.org/10.1039/C2CP42484C

[64] Y. He, L. Zhang, B. Teng, M. Fan, New Application of Z-Scheme Ag_3PO_4/g-C_3N_4 Composite in Converting CO_2 to Fuel, Environ. Sci. Technol. 49 (2015) 649–656, https://doi.org/10.1021/es5046309

[65] Y. Yang, Y. Guo, F. Liu, X. Yuan, Y. Guo, S. Zhang, W. Guo, M. Huo, Preparation and enhanced visible-light photocatalytic activity of silver deposited graphitic carbon nitride plasmonic photocatalyst, Appl. Catal. B 142–143 (2013) 828–837, https://doi.org/10.1016/j.apcatb.2013.06.026

[66] S. Ni, Z. Fu, L. Li, M. Ma, Y. Liu, Step-scheme heterojunction g-C_3N_4/TiO_2 for efficient photocatalytic degradation of tetracycline hydrochloride under UV light, Colloids Surf. A Physicochem. Eng. Asp. 649 (2022) 129475, https://doi.org/10.1016/j.colsurfa.2022.129475

[67] M. Deng, X. Cao, Z. Li, B. Tang, Hybrid triazine-based g-C_3N_4(001)/anatase TiO_2(001) heterojunction: Insights into enhanced photocatalytic mechanism via DFT calculation, J. Photochem. Photobiol. A 423 (2022) 113577, https://doi.org/10.1016/j.jphotochem.2021.113577

[68] I. Altin, X. Ma, V. Boffa, E. Bacaksiz, G. Magnacca, Hydrothermal preparation of B–TiO_2-graphene oxide ternary nanocomposite, characterization and photocatalytic degradation of bisphenol A under simulated solar irradiation, Mater. Sci. Semicond. 123 (2021) 105591, https://doi.org/10.1016/j.mssp.2020.105591

[69] X. Zhang, S.P. Jiang, Layered g-C_3N_4/TiO_2 nanocomposites for efficient photocatalytic water splitting and CO_2 reduction: a review, Mater. Today Energy 23 (2022) 100904, https://doi.org/10.1016/j.mtener.2021.100904

[70] W. Quan, J. Bao, X. Meng, Y. Ning, Y. Cui, X. Hu, S. Yu, H. Tian, 2D/2D Z-scheme photocatalyst of g-C_3N_4 and plasmonic Bi metal deposited Bi_2WO_6: Enhanced separation and migration of photoinduced charges, J. Alloy. Compd. 946 (2023) 169396, https://doi.org/10.1016/j.jallcom.2023.169396

[71] Z. Wu, L. Yang, X. Yang, Y. Gao, X. Liu, M. Que, T. Yang, Z. Liu, H. Zheng, Y. Ma, Y. Li, J. Chen, Synthesis of a novel ternary BiOBr/g-C_3N4/$Ti_3C_2T_x$ hybrid for effectively removing tetracycline hydrochloride and rhodamine B, J. Alloy. Compd. 940 (2023) 168734, https://doi.org/10.1016/j.jallcom.2023.168734